Laser powder bed fusion of immiscible steel and bronze: A compositional gradient approach for optimum constituent combination

Yaojie Wen [a 1], Xiaoke Wu [b 1], Ankun Huang [a], Ramasubramanian Lakshmi Narayan [c], Pei Wang [d], Lijun Zhang [b], Baicheng Zhang [a e], Upadrasta Ramamurty [d f], Xuanhui Qu [a e]

[a] Beijing Advanced Innovation Center for Materials Genome Engineering, Institute for Advanced Material and Technology, University of Science and Technology Beijing, Beijing 100083, China

[b] State Key Laboratory of Powder Metallurgy, Central South University, Changsha, Hunan 410083, China

[c] Department of Materials Science and Engineering, Indian Institute of Technology, Delhi, Hauz Khas, New Delhi 110016, India

[d] IMRE - Institute of Materials Research and Engineering, 2 Fusionopolis Way, Innovis, #08-03, Singapore 138634, Singapore

[e] Beijing Laboratory of Metallic Materials and Processing for Modern Transportation, Beijing 100083, China

[f] School of Mechanical & Aerospace Engineering, Nanyang Technological University, Singapore

Abstract

The microstructures and the mechanical properties of a laser powder bed fusion (LPBF) manufactured alloy coupons that were compositionally graded with austenitic stainless steel 316 L and bronze (Cu10Sn), which are immiscible, were investigated. While the microstructure of the pure 316 L contains only columnar γ-Fe grains, the formation of the equiaxed α-Cu, with α-Fe particles embedded in them, at the grain boundaries of the γ-Fe grains was observed upon alloying with Cu10Sn, for up to 50 wt.%. In the graded alloys with > 50 wt.% Cu10Sn, the microstructure inverts and contains α-Fe particle embedded α-Cu matrix along with some scattered γ-Fe grains. The two-dimensional phase-field simulations were employed to reproduced the phase transition and microstructure evolution in different compositions, revealing that the nucleation of γ-Fe occurs synchronously with the spinodal decomposition of liquid and that with further cooling,

Cu-rich liquid solidifies and nanoscale spherical γ-Fe precipitates appear. Cross-sections with 10–40 wt.% Cu10Sn were found structurally unreliable owing to the formation of liquation cracks and shrinkage pores, whereas the rest of the build contained few pores and was crack-free. The Scheil solidification simulations together with the crack susceptibility index calculations over the entire compositions range of the CGA, reveal that when with < 50 wt.% Cu10Sn, liquid feeding to interdendritic regions of γ-Fe is limited, which is otherwise necessary to mitigate shrinkage-induced stresses. The hardness, yield and tensile strengths of the compositionally graded alloy in the cross-section with 50 wt.% Cu10Sn are higher than those of the parent constituents and the one with 80 wt.% Cu10Sn has the best combination of strength and ductility. The variations in strength and ductility are attributed to the microstructural and compositional changes in α-Cu matrix that were influenced by the formation of α-Fe particles. Finally, the appropriate proportions and the influence of the LPBF method in successfully mixing Cu10Sn and SS316L was discussed.

Graphical abstract

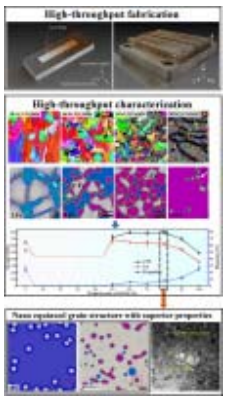

Download: Download high-res image (252KB)
Download: Download full-size image

Keywords

Laser powder bed fusion; Immiscible compositionally graded alloys; High throughput characterization; Ultrafine equiaxed grain; Thermal dynamic calculation

1. Introduction

Mixing copper alloys with a stainless steel is of major technological interest in the power generation, air-conditioning, heat-exchanger, and die-casting industries [1], [2], [3], [4], [5]. This interest is motivated by the possibility of obtaining a material that simultaneously inherits the excellent thermal/electrical conductivity of bronze and the excellent strength and toughness of 316 L [6], [7], [8], [9]. However, attempts to mix Cu alloys and steel presents the following major challenges. First, owing to the high difference in the coefficients of thermal expansions (CTEs) of Cu alloys and steels, large misfit strains and residual stresses will accumulate at the copper alloy-stainless steel interface, which in turn leads to cracking. Second, these two alloys are mutually immiscible in the solid as well as the liquid state, which raises serious concerns regarding the structural integrity of their interface [10], [11], [12], [13], [14], [15], [16], [17]. Third, it was observed that on cooling the molten mixture of the two alloys, steel solidifies first leading to infiltration of liquid copper alloy to its grain boundaries [18], [19], [20]. On solidifying, the copper alloy undergoes shrinkage and causes liquation cracking of the material. Consequently, attempts to mix any combinations of Cu-alloys and steels, using conventional processing methods, such as casting, have been unsuccessful. Alternately, the following studies have attempted to mix Cu and Fe in their pure or alloyed form *via* the laser powder bed fusion (LPBF) technique [21,22]. Zafari and Xia mixed 10, 20 and 50 wt.% Cu in Fe using LPBF and observed that the builds are much stronger than the individual components under compression. They attributed this enhancement in strength of the alloyed builds to the formation of nano-scale Cu precipitates in a Fe matrix. Such nano-scale Cu precipitates facilitate grain refinement of the Fe matrix and act as a barriers for dislocation motion, which leads to the grain boundary (Hall-Petch) and precipitate strengthenings, respectively. However, they reported liquation cracks in all the three builds, which compromise their structural integrity and ability to withstand tensile loads. Liu et al. mixed 8 wt.% Fe and 92 wt.% Cu to avoid the occurrence of liquid phase separation *via* LPBF and the alloy exhibited tensile strength and ductility of ~462.9 MPa and ~30.4 %, respectively [23]. Alternately, Zhou et al. [24] mixed 70 wt.% pure Cu with 30 wt.% 316 L to fabricate a crack-free build *via* LPBF and obtained a tensile strength and ductility of ~590 MPa and ~9 %, respectively. They argued that the enhanced strength is an outcome of grain refinement and precipitation of sub-micron sized Fe phases in the Cu matrix. They also suggested that the successful mixing of the two, otherwise immiscible constituents, is driven by intense Marangoni convection currents generated by the laser power source in LPBF.

While the above studies suggest that Cu and Fe alloys can be mixed via LPBF, the following important questions remain,

i. Only certain specific alloy mixtures, i.e. two compositions with higher proportions of Fe (~90 and 80 wt.%), one composition with relatively higher Cu (~70 wt.%) content and one with equal contents of Fe and Cu have been studied previously. Then it is worth asking if there are other combinations of the two alloys that can be mixed to obtain a crack-free build with excellent mechanical properties?
ii. It is evident that builds that have compositions with relatively higher Fe content contain liquation cracks, whereas that with 70 wt.% Cu is crack-free. What

is the underlying reason for this variation in cracking tendency of these compositions?

iii. The above-mentioned studies highlight that despite Cu and Fe undergoing phase separation in the liquid phase, they form unique microstructures when mixed and fabricated via LPBF. It is then imperative to understand how the microstructure and phases evolve when the alloy mixture melts and subsequently solidifies within the melt-pool during LPBF. Also, what are the unique conditions in LPBF processing that facilitate the mixing of the two otherwise immiscible constituents?

A particularly attractive way to answer these questions is through the fabrication of a compositionally graded alloy (CGA) of Cu and Fe alloys by varying their relative proportions along the length of the built coupon. In several prior studies, CGAs were built vertically, such that the composition gradient is aligned along the build direction. However, it was observed that the CGAs developed by this method have large compositional fluctuations along the gradient and are also prone to cracking [25], [26], [27]. Alternately, to mitigate these issues, we developed a powder dispensing strategy, which introduces composition gradient along the horizontal direction or in the plane of the powder bed. By employing this method, we have successfully produced crack-free and highly dense builds of CoCrMo/IN718 and IN718/SS316L CGAs, and both have smooth compositional gradients [28,29].

In the present study, with the aim of assessing the feasibility of alloying different proportions of Cu10Sn (bronze) and SS316L via LPBF, we fabricated a Cu10Sn/SS316L CGA, by employing the above-mentioned build strategy. While bronze has the lowest thermal conductivity amongst the Cu alloys, these two alloys were specifically chosen to represent a model CGA system of Cu alloys and steels as their constituent elements, Cu, Sn and Fe, Cr, Ni, Mn, Mo, respectively, are mutually immiscible. It should however be noted that the results of this study would broadly extend to other Cu alloy/steel combinations as well, provided they are individually printable by LPBF. This was followed by a detailed characterization of the composition, microstructure, and mechanical properties of different cross sections in the CGA. To understand the constituent phases in the microstructure of different portions in the build, complementary simulations were run on CALPHAD (Calculation of Phase Diagrams), to calculate the phase diagram of the Cu10Sn-SS316 system. Moreover, the phase field simulations using the multi-phase field (MPF) model were performed to understand the phase evolution in the CGA with different microstructural length scale. From the present experimental results, it was determined that crack free, high-density and high-strength alloys of Cu10Sn and SS316L can be produced via LPBF, provided they contain ≥ 50 wt.% of Cu10Sn. To discern the cracking tendency of other cross-sections, the mathematical framework for solidification cracking, developed by Kou [30], was integrated with the Scheil-Gulliver solidification simulations in the CALPHAD framework. Finally, discussions on the microstructural features that influence different mechanical properties of alloys with different compositions are presented. The discussions are expected to provide insights on choosing the appropriate proportions of Cu alloys and steels to develop alloys with excellent thermal/electrical functionality as well as good structural integrity.

2. Experiments and methods

2.1. Powder dispensing system and CGA samples preparation

The CGA samples were created using an in-house developed LPBF system that was integrated with a custom designed continuous gradient powder feeding device. The LPBF system has a 500 W fiber laser, which has a wavelength of 1070 nm and a spot size (diameter) of 35 μm. More details of the functions of the continuous gradient powder feed setup are provided in our previous paper [28]. In this study, Cu10Sn and SS316L were selected for fabricating the CGA. A schematic of the powder delivery strategy and the fabrication process of the CGA are shown in Fig. 1**(a) and (b)**. The representative images of the Cu10Sn-SS316L CGA builds are shown in Fig. 1**(c).** Three builds with dimensions, 50 × 110 × 6 mm^3, 10 × 110 × 6 mm^3 and 20 × 110 × 6 mm^3 ($X \times Y \times Z$), were fabricated. At the two extremities of the build, which are labelled as "SS316L" and "Cu10Sn" in Fig. 1(**c**), regions spanning 15 mm contain pure SS316L and Cu10Sn, respectively. The region in between these extremities, which spans 80 mm and is labelled as the "gradient range" in Fig. 1**(c)**, contains the compositionally graded SS316L-Cu10Sn alloy. Laser parameters, such as power, scan speed, hatch distance and thickness, are significantly different for fabricating dense builds of pure SS316L and Cu10Sn owing to the dissimilarities in their thermophysical properties. Therefore, a systematic optimization study is conducted *a priori* to determine appropriate process parameters for fabricating the CGA build with different proportions of Cu10Sn and SS316L. The determined process parameter combinations for fabricating crack free, pure Cu10Sn and SS316L and their mixtures are listed in Table 1. Note that in all cases, the layer thickness was fixed as 30 μm.

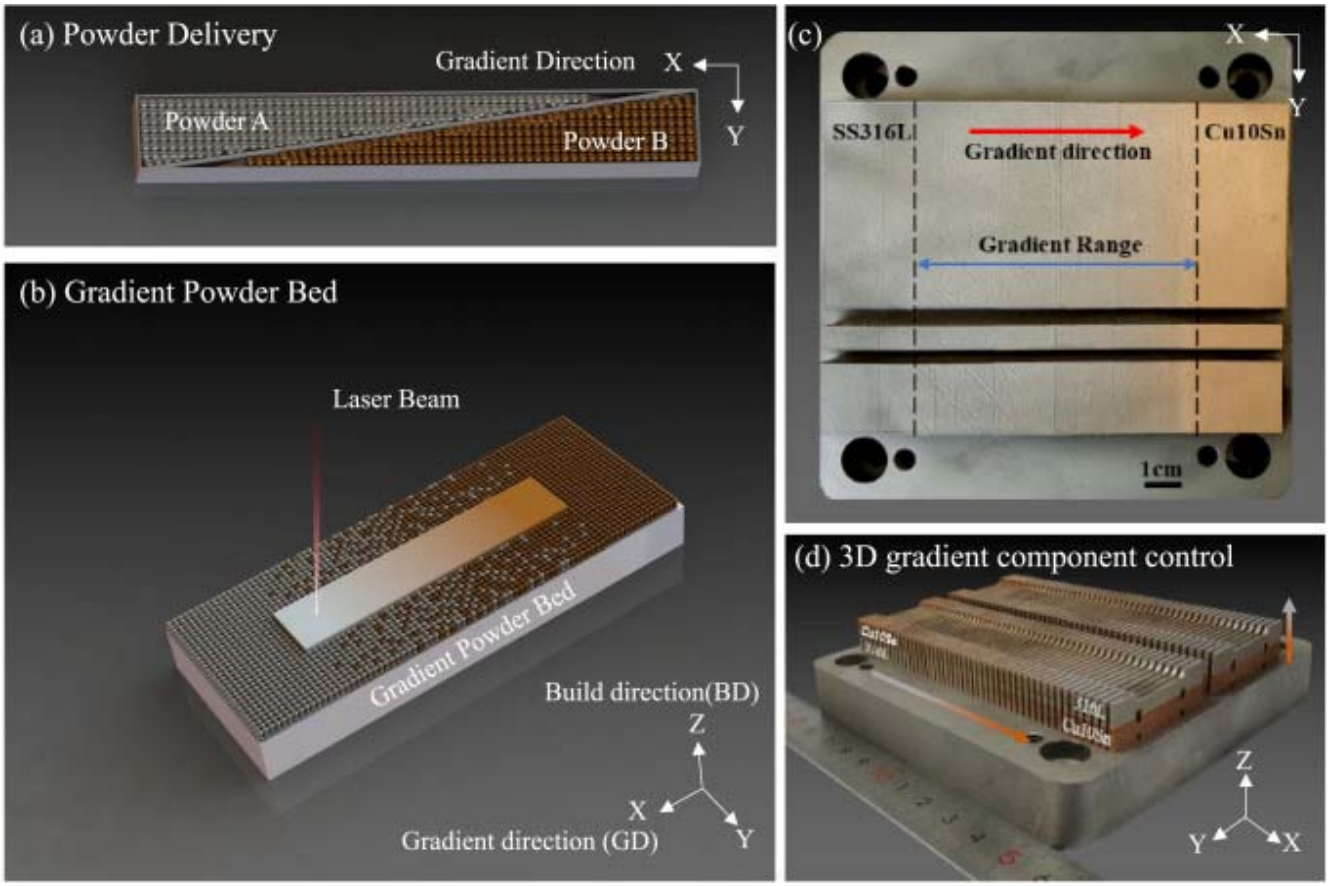

1. Download: Download high-res image (967KB)
2. Download: Download full-size image

Fig. 1. Schematic illustration for (a) the powder delivery and (b) the fabrication process of the CGA. (c) Optical images of the SS316L/Cu10Sn CGA build, and (d) the tensile test coupons of SS316L/Cu10Sn CGA.

Table 1. Laser parameters for fabricating the Cu10Sn/SS316L CGA.

Empty Cell	**100 % 316L**	**100 %–80 % 316L**	**80 %–60 % 316L**	**60 %–40 % 316L**	**40 %–20 % 316L**	**20 %–0 % 316L**	**100 % Cu10Sn**
Laser Power (W)	260	275	275	290	315	350	350
Scan Speed (mm/s)	960	960	850	750	600	500	450
Hatch Distance (μm)	90	90	100	100	120	140	140

2.2. Feedstock powder materials

Gas atomized, spherical powders of SS316L and Cu10Sn, with particle sizes in the range of 15–53 μm were used in this study. Table 2 lists the compositions of the two powders
Table 2. Chemical composition of Stainless Steel 316 L and Cu10Sn powders (in wt.%).

316L	**Fe**	**Cr**	**Ni**	**Mn**	**Mo**	**O**	**Si**	**C**
	Bal.	**16.8**	**12.1**	**1.87**	**2.25**	**0.12**	**0.03**	**0.02**
Cu10Sn	Cu	Sn						
	Bal.	10.09						

2.3. Characterization

For performing the microstructural characterization, the cross section slices were cut along the gradient direction (GD) from the Cu10Sn-316 L CGA. These slices were ground and polished to a mirror finish as per the ASTM E3–11 standard [31]. After etching the polished slices with 0.5 g $FeCl_2$ + 10 ml C_2H_5OH + 10 ml HCl for 20–40 s, they were observed under a scanning electron microscope (SEM, Hitachi FE-SEM SU8000). Phase analysis was conducted using X-ray diffraction (XRD, Rigaku Ultima-IV) with Cu Kα radiation. Chemical composition maps of the CGAs were measured via energy dispersive spectroscopy (EDS, Bruker). EDS measurements were made on 40 locations along the GD at equally spaced intervals of 2 mm. At each location, 3 measurements were made to ensure repeatability. To obtain more detailed microstructural information, electron backscatter diffraction (EBSD, HKL Nordlysnano) and transmission electron microscopy (TEM, FEI TECNAI G2 F20) were also employed.

Microhardness and tensile properties were also measured on different cross sectional slices extracted along GD of the CGA. A microindenter equipped with a Vickers tip was used for measuring the microhardness. A maximum load of 200 g and a dwell time of 10 s was employed for each measurement. Tensile tests were performed at room temperature on a CMT4105 universal testing machine according to the ASTM-E8 standard [32]. Several flat dog-bone shaped plate samples were extracted from different locations along the GD, from the 50 × 100 × 6 mm^3 CGA builds. Fig. 1**(d)** displays the tensile test coupons of SS316L/Cu10Sn CGA that were utilized in the study. These samples have a gauge length of 20 mm and thickness of 1.5 mm and the loading direction was always perpendicular to GD.

2.4. Solidification simulations

To understand the process of solidification, the Scheil-Gulliver solidification simulations were performed [33,34] using the Thermo-Calc software, which is equipped with the TCCU3 thermodynamic database. For this purpose, 83 combinations of Cu10Sn/SS316 alloy mixtures, representing different sections of the CGA along the GD, are chosen uniformly over the entire gradient composition space for the simulations. To evaluate the cracking tendency of different sections during solidification, the mathematical model developed by Kou [30,35] was employed in this study. During the solidification of alloys, solidification shrinkage and thermal contraction of the semi-solid regions, referred to as mushy zones, occurs. This shrinkage is constrained by the rigid substrate or

previously solidified layer to which the melt pools are attached. This constraint in shrinkage introduces tensile loads in the mushy zone. The mushy zone, which contains grains that are not bonded well and are separated by liquid, has poor mechanical strength and ductility. Therefore, during the final stages of solidification, the fraction of liquid, f_L, is not sufficient to allow grains to rearrange themselves and accommodate the shrinkage-induced tensile stresses, which leads to the formation of cracks at grain boundaries. Kou [30,35] developed a mathematical framework to understand the different variables involved in this process and developed a relative measure referred to as the crack susceptibility index (CSI), which is defined as,

$$\mathrm{CSI} = \left| dT/d(f_s)^{1/2} \right|_{\mathrm{Max}} \quad (1)$$

where dT is the change in temperature and fs is the fraction of solid phases, which can be obtained for different sections in CGA via the Scheil-Gulliver solidification simulations described above.

2.5. Multi-phase-field simulation

In the multi-phase-field (MPF) model for the solidification process, the total energy functional consists of the interfacial energy density f^{intf} and chemical energy density f^{chem} [36],

$$F = \int_{\Omega} f^{\mathrm{intf}} + f^{\mathrm{chem}} \quad (2)$$

$$f^{\mathrm{intf}} = \sum_{\alpha,\beta=1,\ldots,N,\alpha\neq\beta} \frac{4\sigma_{\alpha\beta}}{\eta_{\alpha\beta}} \left\{ -\frac{\eta_{\alpha\beta}^2}{\pi^2} \nabla\phi_\alpha \cdot \nabla\phi_\beta + \phi_\alpha \phi_\beta \right\} \quad (3)$$

$$f^{\mathrm{chem}} = \sum_{\alpha=1,\ldots,N} h\left(\phi_\alpha\right) f_\alpha\left(c_\alpha^i\right) + \tilde{\mu}^i \left(c^i - \sum_{\alpha=1}^{N} \phi_\alpha c_\alpha^i \right) \quad (4)$$

where F is the total energy, Ω is the entire simulation domain, N is the local number of phases/grains with the sum constraint $\sum_{\alpha=1}^{N}\phi_\alpha=1$. ϕ_α is the phase field of α phase/grain which equals to the phase/grain fraction. $\sigma_{\alpha\beta}$ and $\eta_{\alpha\beta}$ are the interfacial energy and interface thickness for the α/β interface, respectively. $h(\phi_\alpha)$ is a monotonic interpolation function for coupling. $f\alpha(c_\alpha^i)$ is the bulk free energy density of the individual phase α, which depends on the temperature T as well as the phase concentration cαi. μ˜i is the diffusion potential for element i which is applied as a Lagrange multiplier for the mass conservation of element i. ci is the total concentration of element i.

Based on the above energy functional, the evolution function for the phase field as well as the concentration field are derived as follows,

$$\dot{\phi}_\alpha = \sum_{\beta=1}^{N} \mu_{\alpha\beta} \left\{ \sigma_{\alpha\beta} \left[\phi_\beta \nabla^2 \phi_\alpha - \phi_\alpha \nabla^2 \phi_\beta + \frac{\pi^2}{2\eta_{\alpha\beta}^2} (\phi_\alpha - \phi_\beta) \right] + \frac{\pi}{\eta_{\alpha\beta}} \sqrt{\phi_\alpha \phi_\beta} \Delta G_{\alpha\beta} \right\} \quad (5)$$

$$\Delta G_{\alpha\beta} = \Delta G_{\alpha\beta}^{\text{chem}} = f_\beta \left(c_\beta^i \right) - f_\alpha \left(c_\alpha^i \right) + \tilde{\mu}^i \left(c_\alpha^i - c_\beta^i \right) \quad (6)$$

$$\dot{c}^i = \nabla \sum_{\alpha=1}^{N} \phi_\alpha \widetilde{M}_\alpha \nabla \tilde{\mu}_\alpha^i = \nabla \sum_{\alpha=1}^{N} \phi_\alpha \widetilde{D}_\alpha \nabla c_\alpha^i \quad (7)$$

where $\mu_{\alpha\beta}$ is the interface mobility for the α/β interface, $\Delta G_{\alpha\beta}$ is the total driving force for α/β interface and equal to the chemical driving force, $\Delta G_{\alpha\beta}^{chem}$, in solidification process. $\tilde{M}_\alpha$ and $\tilde{D}_\alpha$ are the chemical mobility and interdiffusivity for the element *i* in phase α.

The OpenPhase code [37], an open-source phase-field simulation code package developed in the formalism of MPF model, was utilized for running the present simulations. First, in order to study the microstructure evolution of the CGA at the microscopic scale with the OpenPhase code, four sets of two-dimensional (2-D) MPF simulations were performed in a domain of 100 × 100 μm^2 with the grid spacing as Δx = 0.5 μm. Four reference compositions, 20, 40, 60 and 80 wt.% Cu were chosen. Second, in order to study the nucleation and growth behavior of the nano γ-Fe particle during the LPBF process, one set of 2-D MPF simulation of the CGA in nanoscale was performed based on the microstructure generated from the phase-field simulation results in the microscopic scale of the CGA with 80 wt.% Cu. The simulation domain has a dimension of ~22 μm^2 and a grid spacing of Δx = 0.01 μm. Periodic boundary conditions were set for both phase field and concentration field. The thermodynamic database, TCCU3, was coupled with the MPF simulation through the linear phase diagram scheme [38,39]. Also, the temperature-dependent and composition-dependent interdiffusivity for both liquid and γ-Fe phases were also applied in the present phase-field simulation. More details of the MPF simulations are provided in SI.

3. Results

3.1. Composition and phase distribution in SS316L-Cu10Sn CGA

The chemical composition variations of the SS316L-Cu10Sn CGA along the gradient direction were measured with EDS. Fig. 2 shows the distributions of the seven main elements, Cu, Sn, Fe, Cr, Ni, Mn, and Mo in wt.%, along the GD in the CGA. For comparison, the expected composition distribution is also included in the same plot in the form of straight lines. Note that each experimentally measured data point represents the average composition over an area of 1 × 1 mm^2 on cross sections extracted along GD. A good agreement between the expected and experimentally measured composition distribution indicates that the chosen laser parameters were appropriate.

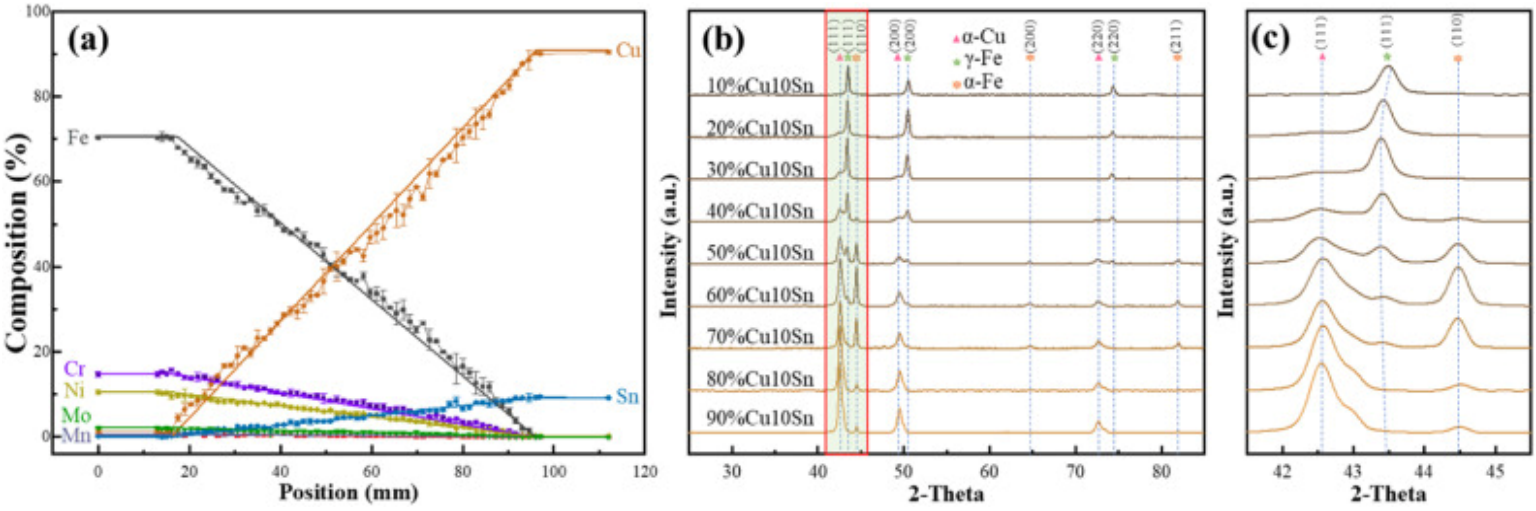

1. Download: Download high-res image (467KB)
2. Download: Download full-size image

Fig. 2. (a) Chemical composition distribution of primary elements, measured along GD via EDS. (b) XRD patterns of different cross-sections along the GD of the SS316L/Cu10Sn CGA, and (c) the amplification from 41.5°–45.5°

XRD scans of cross-sections with 10–90 wt.% of Cu10Sn, extracted along the GD of the SS316L-Cu10Sn CGA are shown in Fig. 2**b**. In the cross section with 10 wt.% Cu10Sn, prominent peaks corresponding to (111), (200), and (220) planes of the face centered cubic (FCC) γ-Fe phase were identified. Moreover, a faint shoulder close to the (111) peak of γ-Fe, which corresponds to the FCC α-Cu phase, was also observed in the scan. Note that although γ-Fe and α-Cu have the same crystal structure, their diffraction peaks do not exactly coincide, due to the differences in their unit cell sizes [40,41]. In the XRD scans of cross sections with 30 wt.% Cu10Sn, this shoulder becomes more prominent. Furthermore, for cross sections with > 40 wt.% Cu10Sn, the peak corresponding to α-Cu becomes distinct, and increases in intensity with an increase in the wt.% Cu10Sn. Concurrent to the increase in the intensity of α-Cu peaks, there is a steady decrease in the intensity of γ-Fe peaks, followed by its complete disappearance in cross-sections with > 70 wt.% Cu10Sn. Instead, the (110) peak of the body centered cubic (BCC)

α-Fe, which is otherwise absent in sections with up to 40 wt.% Cu10Sn, increases in intensity with increasing Cu10Sn content. However, in cross sections with > 80 wt.% Cu10Sn, the intensity of the α-Fe peaks drops significantly. These observations suggest that cross sections with >70 wt.% SS316L, are predominantly comprised of the γ-Fe phase. However, with increase of Cu10Sn (in wt.%) in the CGA, the α-Cu and α-Fe phase contents increase while that of γ-Fe decreases. In the cross-sections with > 80 wt.% Cu10Sn, a shoulder is observed in the (111) diffraction peak of α-Cu. Tentatively, the appearance of this shoulder could be attributed to the formation of the δ-Cu phase, of which (660) peak partially overlaps with the (111) peak of α-Cu [41]. Alternately, the shoulder could also be an outcome of the poor miscibility of Sn and Fe, owing to their significant size differences, which may lead to peak broadening.

3.2. Microstructure evolution

Fig. 3**a** show the representative low magnification images of sections with the composition of 10–90 wt.% Cu10Sn along the GD in the BD-GD plane of the SS316L-Cu10Sn CGA. In all cross-sections, the microstructure contains two phases, one with dark contrast and the other with bright contrast. The variations in the area fractions of the two phases in the CGA, along the GD, are represented in the form of a bar chart in Fig. 3**b.** With increasing wt.% of Cu10Sn in the CGA, the area fractions of the bright phase gradually increase and that of the dark phase decreases. The elemental distribution maps of sections with 25, 50 and 75 wt.% Cu10Sn are shown in **Fig. S1.** Within each individual section, the spatial distributions of Fe, Ni, Cr and Mo are nearly identical. Similarly, locations with high concentration of Sn coincide with that of Cu (see **Fig. S1**). Based on the back-scattered electron (BSE) images and EDS mapping, it can be deduced that the bright phases are Cu10Sn-rich and the dark phases are SS316L-rich phases. The composition of both phases in different sections was measured by EDS and listed in **Table S1**. The Fe and Cu content in the dark and bright phases, represented by hollow squares and hollow circles, respectively, within these sections is plotted in Fig 3**b**. From this plot, it is evident that, in general, the dark phase is rich in Fe but lean in Cu, whereas the converse is true in the bright phase.

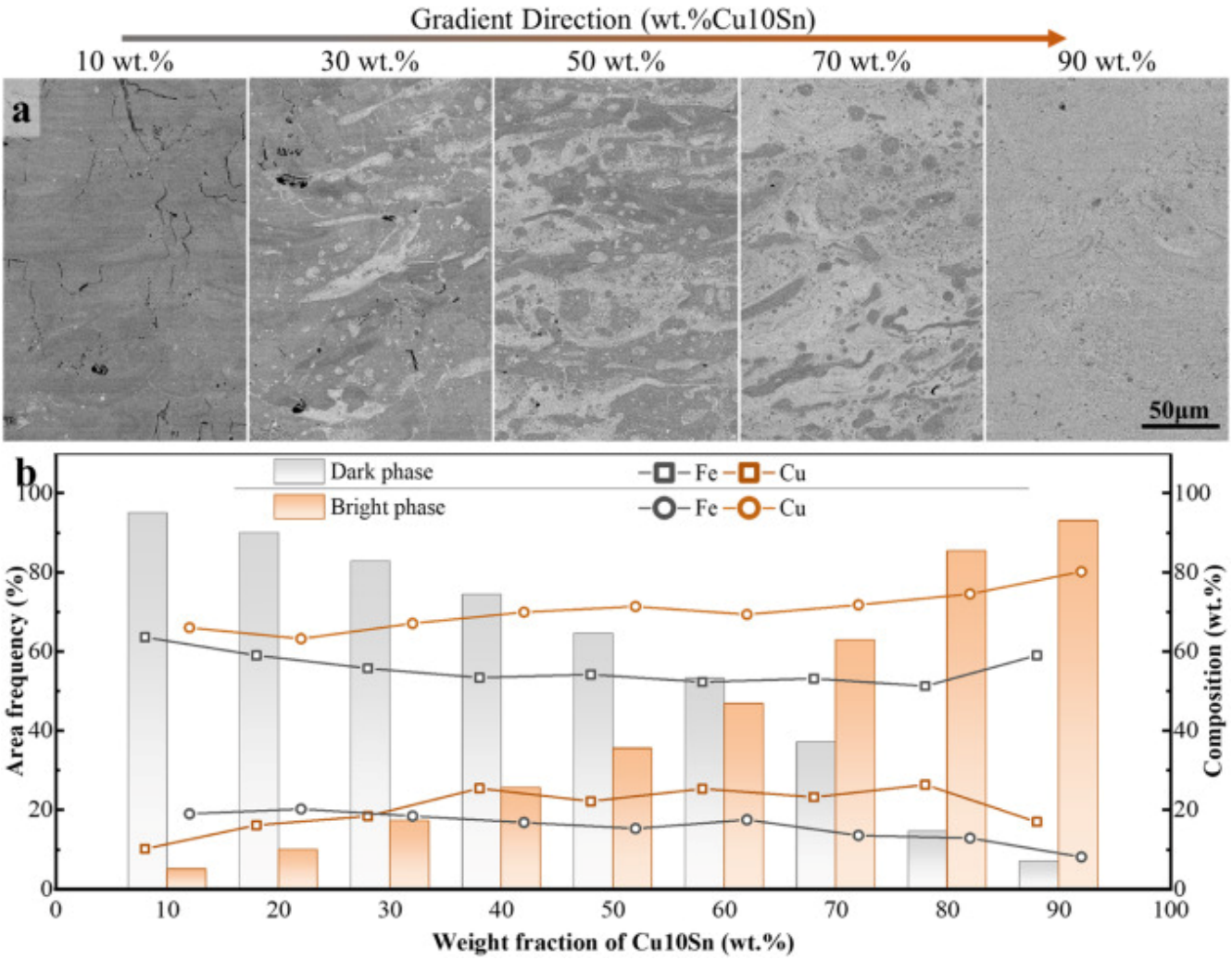

1. Download: Download high-res image (1MB)
2. Download: Download full-size image

Fig. 3. Representative high magnification BSE image of sections with (a) 10–90 wt.% Cu10Sn in the CGA. (b) The area fractions of the dark and bright phases and the wt.% of Fe and Cu in cross-sections of the CGA.

In the section with 10 wt.% Cu10Sn, several pores and cracks were observed. The number density of cracks, N_c, which is defined as the number of cracks per unit area, and area fraction of pores, A_p, determined by image analysis, are 6.62 mm^{-2} and 0.39 %, respectively (see for example, **Fig. S2**). With an increase in the content of Cu10Sn to 20 wt.% in the CGA, N_c decreases to 4.86/mm^{-2} and A_p increases to 0.59 %, respectively. N_c further decreases to 3.99 mm^{-2} and A_p further increases to 1.51 % in the cross-section with 30 wt.% Cu10Sn. In the cross-section with 40 wt.%, N_c and A_p both decrease to 0.86 mm^{-2} and 0.77%, respectively. However, while cross-sections with 50 wt.% Cu10Sn are crack free, A_p in them is ~0.55 % (see also Fig. S2). Similarly, cross-sections with > 50 wt.% Cu10Sn are fully dense, in addition to being crack-free. Careful examination of the EDS maps (see **Fig. S1)** reveals that locations surrounding the cracks (indicated by white arrows) in slices with 10–30 wt.% Cu10Sn are enriched with Cu.

Higher magnification images of the cross-sections with 20, 40, 60 and 80 wt.% Cu10Sn are shown in Fig. 4. It is evident that in all of them, the dark (Fe-rich) and bright (Cu-rich) phases contain dispersed spherical precipitates of bright and dark contrast, respectively. This implies that these spherical precipitates are enriched with Cu and Fe, respectively.

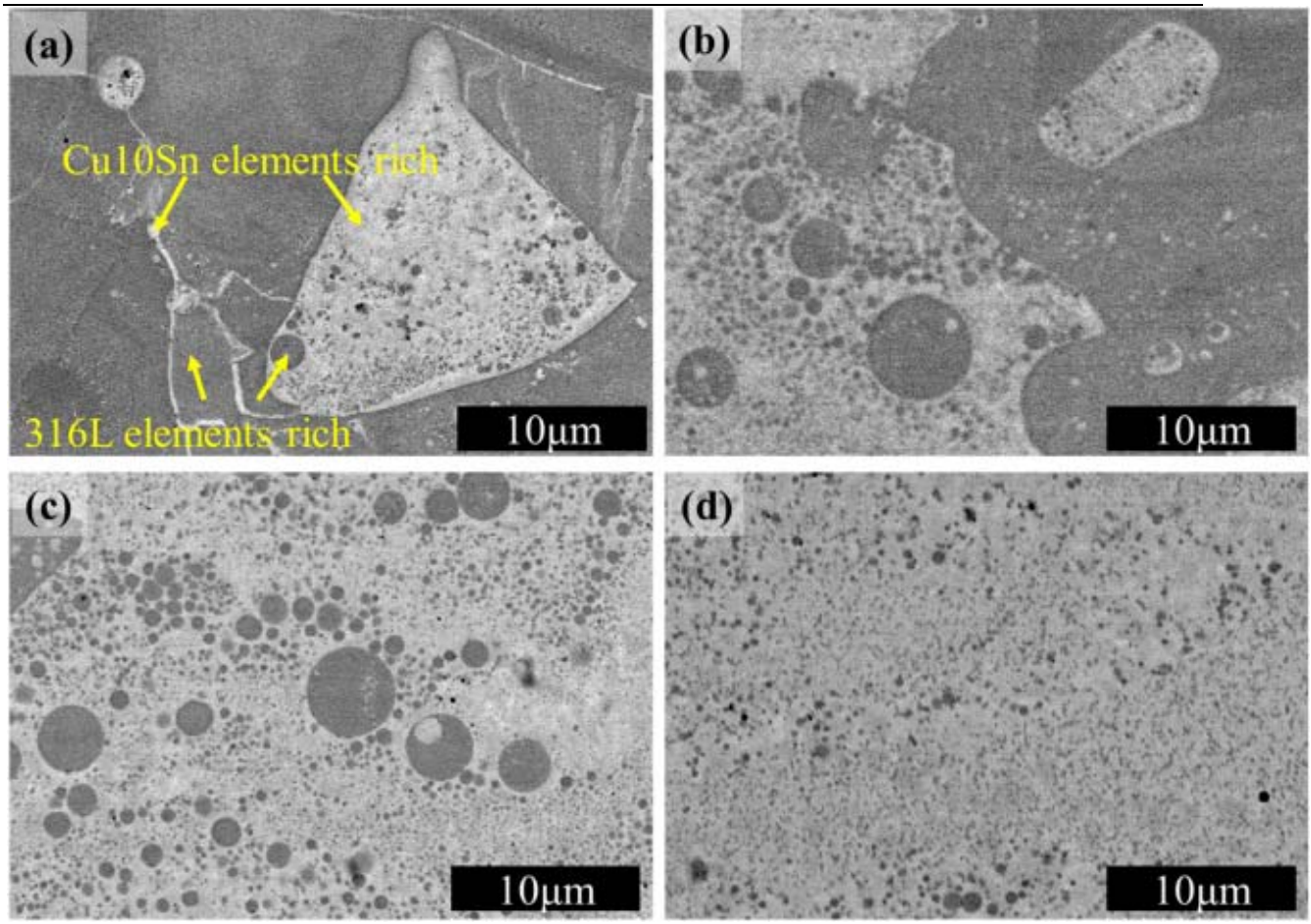

1. Download: Download high-res image (1MB)
2. Download: Download full-size image

Fig. 4. High magnification images of the cross-sections with 20, 40, 60 and 80 wt.% Cu10Sn.

To further understand the microstructural evolution of the CGA, higher resolution SEM and EBSD characterization was performed on different slices along the GD in the BD-GD plane. **Fig. S3** shows the representative EBSD images of cross-sectional slices with 0 and 100 wt.% Cu10Sn. Both of them contain columnar grains which have average widths of 37.58 and 3.78 μm (with the aspect ratios are 3.98 and 1.81), respectively. In Fig. 5**(a1)–(d1)** the representative IPF-Y0 (Inverse Pole Figure) maps of slices with 20, 40, 60 and 80 wt.% Cu10Sn, respectively, are displayed. The corresponding phase maps and {001} pole figures of these slices are shown in Fig. 5**(a2)–(d2)** and **(a3)–(d3)**, respectively. In the cross-section with 20 wt.% Cu10Sn, the microstructure consists of both columnar and equiaxed grains. While the columnar grains are 14.2 ± 15.6 μm wide (an aspect ratio of 2.8 ± 1.4), the width of the equiaxed grains

could not be accurately measured due to their small size. IPF maps and pole figures indicate that the overall microstructure has a ⟨001⟩ texture along the BD and phase maps indicate the presence of a FCC phase (red color). It is also observed that some regions at the grain boundaries (indicated by white arrows) are not detected in the EBSD scans. Based on the high intensity of the γ-Fe peaks in the XRD scans of this cross-section (see Fig. 2), it is evident that both columnar and equiaxed grains are the γ-Fe phase. Since XRD scans also indicate that traces of the α-Fe and α-Cu phases are also present in this cross-section, they are expected to be present in the above-mentioned unmapped regions at the grain boundaries. In the cross-section with 40 wt.% Cu10Sn, the microstructure becomes fully equiaxed and the average grain size is 20.7 ± 13.4 μm. Moreover, as observed in the section with 20 wt.% Cu10Sn, these γ-Fe have a ⟨001⟩ texture. However, note that the extents of the undetectable regions close to the grain boundaries are larger in this section.

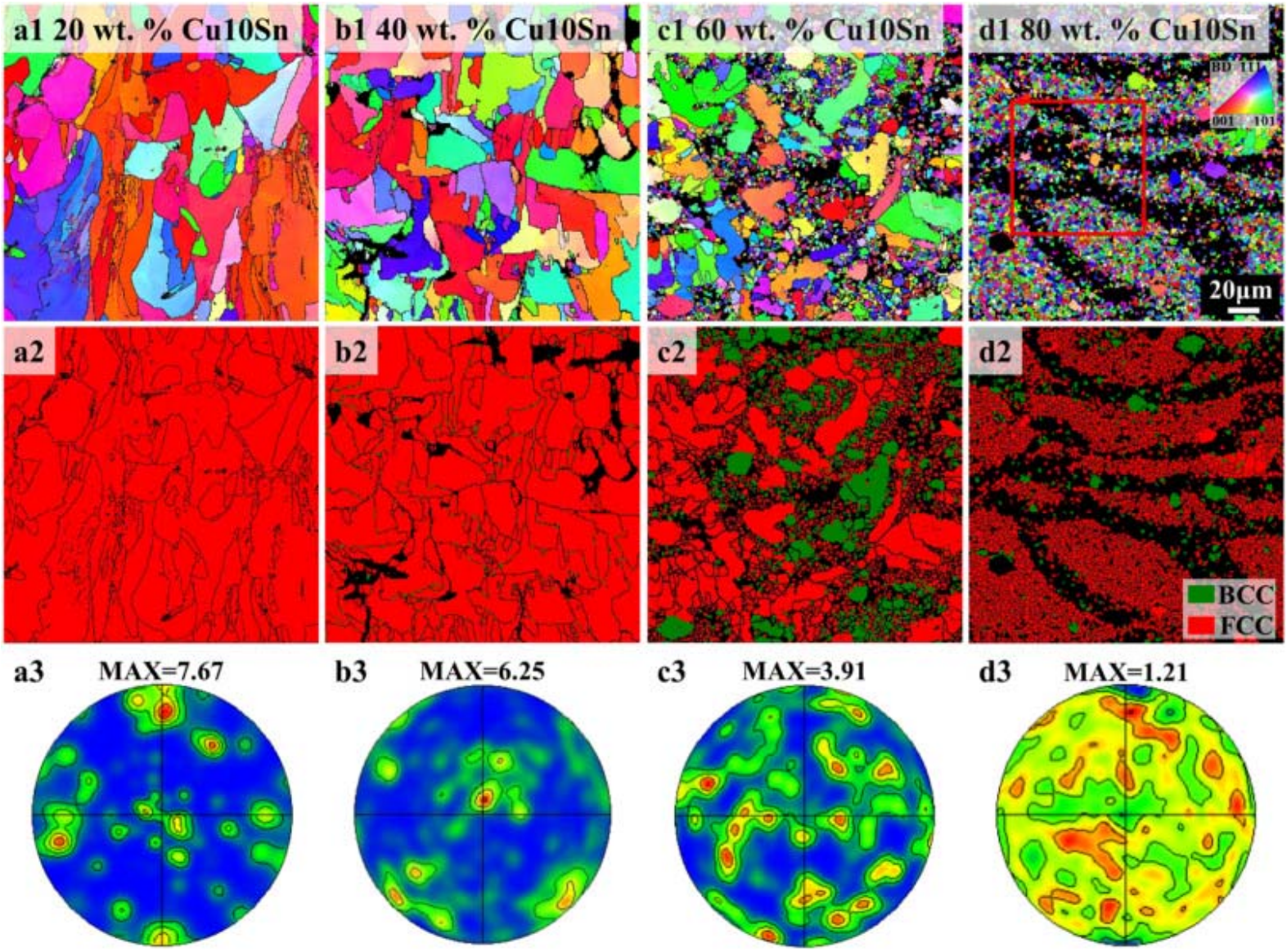

1. Download: Download high-res image (3MB)
2. Download: Download full-size image

Fig. 5. Representative inverse pole figure Y0 (IPF-Y0) maps of the CGA in cross-sections with (a1) 20 wt.% Cu10Sn, (b1) 60 wt.% and (c1) 80 wt.% Cu10Sn. (a2-c2) corresponding phases maps and (a3-c3) {001} pole figure of FCC phase of these cross-sections.

In the cross-section with 60 wt.% Cu10Sn, while the microstructure becomes fully equiaxed, the grain size distribution becomes bimodal as several fine grains are observed along with coarse grains. The average sizes of the large and fine grains are 13.1 ± 2.6 μm and 1.18 ± 0.58 μm, respectively. Combining the observations from phase maps and XRD scans, it is deduced that the large grains are mostly composed of an FCC phase, which could either be α-Cu phase or the γ-Fe phase or a mixture of both. The fine grains are mostly the α-Fe (BCC) phase. Both the phases have a random texture, as can be seen in the IPF maps. In contrast, in the section with 80 wt.% Cu10Sn, the microstructure predominantly consists of the randomly textured, 1.27 ± 0.64 μm sized equiaxed fine grains of the FCC phase and few 10 μm sized coarse grains of the BCC phase. XRD scans suggest that this FCC phase is most likely α-Cu, whereas the BCC phase is α-Fe.

Much like that observed in the section with 20 and 40 wt.% Cu10Sn, several unidentifiable regions (indicated by white arrows) in the EBSD scans were observed in sections with 60 and 80 wt.% Cu10Sn. In fact, these undetected regions coincide with the previously identified contiguous bright phase, which contains dispersed spherical particles that have bright contrast. It is likely that the EBSD scanning in these regions are unsuccessful because the microstructure in these regions is finer than the step size of the EBSD scans, which is ~ 0.7 μm. To visualize the microstructure in these dark regions, high resolution SEM (see Fig. 4) and TEM imaging of sections with 60 and 80 wt.% Cu10Sn is performed and the step size for EBSD scans is reduced to 30 nm. Unfortunately, due to the presence of grain boundary cracks in the cross-sections with 20 and 40 wt.% Cu10Sn, its high resolution EBSD scanning was not possible.

Fig. 6**(a)** displays the EBSD IPF-Y0 map of the previously undetected regions (within red box in Fig. 5**(d1)**) in section with 80 wt.% Cu10Sn. These regions are 20 μm wide continuous bands that contain finer grains than those in the surrounding regions. From the curvature of these bands, it is determined that they are melt-pool boundaries and the regions surrounding them are the interiors of the melt-pool. The EBSD IPF-Y0 map of the melt-pool boundary (enclosed within the dashed yellow box b in Fig. 6(a)), shown in Fig. 6**(b)**, indicates that these fine grains have random texture. Phase maps of the melt pool interior and boundaries are shown in **Fig. S4(a) and (c)**. In both the regions, while most grains are the FCC phase, there are also few grains of the BCC phase. From the plots of grain size distribution, shown in **Fig. S4(b) and (d)**, it is determined that the average sizes of the grains in the melt pool interior and those at the melt pool boundaries are 1.18 ± 0.58 μm and 0.35 ± 0.13 μm, respectively.

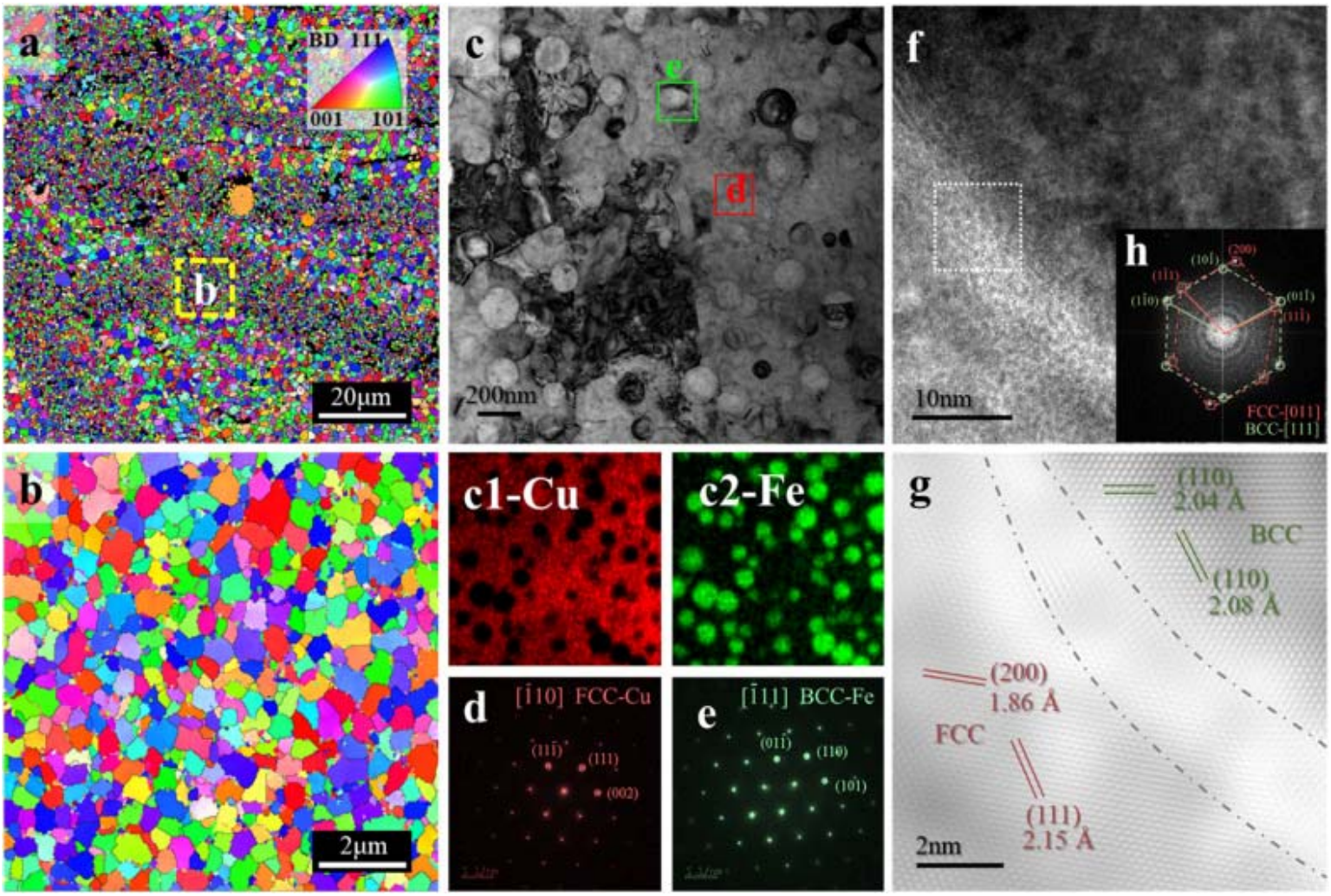

1. Download: Download high-res image (2MB)
2. Download: Download full-size image

Fig. 6. (a) IPF Yo map of cross section with 80 wt.% Cu10Sn and (b) IPF Yo map of the melt pool boundaries extract from (a). (c) Bright field images of the microstructure and EDS mapping of the matrix and spherical. Representative SAED pattern of the (d) α-Cu matrix and (e) α-Fe spherical particle. (f) HRTEM image of the α-Cu matrix and α-Fe spherical particle interface, and corresponding (g) IFFT and (h) FFT images.

To further characterize the phases in the microstructure, TEM analysis of the melt-pool regions is performed. Bright field TEM image of the melt-pool interior is shown in Fig. 6**(c)**, respectively. In this region, spherical phases, which have a lighter contrast, are found embedded within the matrix. While a similar microstructure is observed at the melt-pool boundaries (shown in **Fig. S5**), the average size of the spherical phases in it are 154.7 ± 21.9 nm whereas that in the interior is 187.3 ± 36.1 nm. Fig. 6**(c1) and (c2)** show the Cu and Fe EDS maps, whereas Fig. 6**(d) and (e)** show the EDS maps and SAED patterns of the spherical phase and the matrix, respectively. From these, it is evident that the matrix is the FCC α-Cu phase and the spherical particles are the BCC α-

Fe phase. The high-resolution TEM image of the spherical phase and matrix, shown in Fig. 6**(f) and (g)**, indicates that their interface is incoherent. The incoherence of the nanoscale precipitates with the matrix suggests that they did not form as a result of solid-state precipitation. Based on these observations, we believe that the phase with light contrast observed in magnified SEM images of all cross-sections shown in Fig. 4, contains α-Fe spherical particles embedded in the α-Cu matrix.

Overall, while the microstructures of 0 and 100 wt.% Cu10Sn are columnar and dendritic, the rest of the CGA has microstructural features whose length scales vary from tens to hundreds of microns to a few hundred nanometers. In the cross sections with ≤ 40 wt.% Cu10Sn, the matrix consists of columnar and equiaxed γ-Fe grains whereas a mixture of α-Cu as a matrix and α-Fe in the form of spherical precipitates exist at the grain boundaries. Moreover, several cracks were also observed at the grain boundaries in these sections. However, when 60 wt.% of Cu10Sn is present in the CGA, the microstructure changes dramatically to a fine, equiaxed, α-Cu matrix with several embedded spherical α-Fe precipitates and isolated large grains of γ-Fe and α-Fe. With a further increase in the wt.% of Cu10Sn in the CGA, the matrix consists of only α-Cu grains with spherical α-Fe precipitates. The size of α-Cu grains and α-Fe precipitates is finer in the melt-pool boundaries compared to that in the melt-pool interior.

3.3. Calculated phase diagram of Cu10Sn-SS316L

Considering Cu, Fe, Cr and Ni as the representative constituents of Cu10Sn and SS316L, the pseudo-binary equilibrium phase diagram, calculated using the Thermol-Calc software in the framework of CALPHAD approach, for the Cu10Sn-SS316L system is shown in Fig. 7. For the composition range with 30–85 wt.% Cu10Sn, there is a miscibility gap in the liquid state above 1600 K. The critical point of the immiscibility limit is observed at 1750 K and composition of 65 wt.% Cu10Sn, above which the alloy forms a homogeneous liquid solution, L. Below the limit of immiscibility, L separates into two liquids, L_{Cu} and L_{Fe}, which are rich in Cu and Fe, respectively. Also, a monotectic reaction, which results in the formation of the SS316L rich FCC phase (γ-Fe), is observed at 1600 K for the composition with 30 wt.% Cu10Sn. For compositions with 10–85 wt.% Cu10Sn, γ-Fe, L_{Cu} and L_{Fe} are in equilibrium below the monotectic reaction isotherm and above the liquidus line at 1550 K. Below this liquidus line, for the same composition range, L_{Fe} fully transforms to γ-Fe and is in equilibrium with L_{Cu}. There is another liquidus line at 1400 K, below which, L_{Cu} finally transforms to α-Cu, and is in equilibrium with γ-Fe up to 870 K. Finally, a solid-state transformation, where γ-Fe partially transforms to α-Fe, is observed to occur below 870 K, such that γ-Fe, α-Cu and α-Fe co-exist at room temperature.

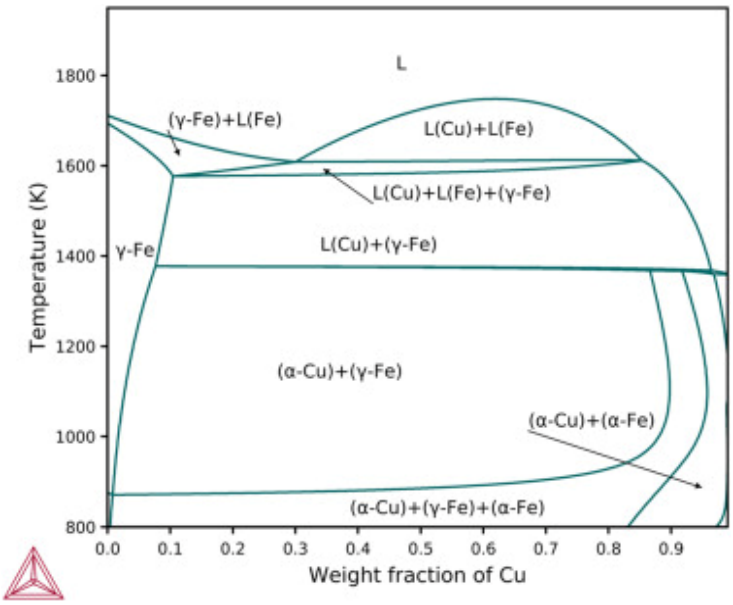

1. Download: Download high-res image (177KB)
2. Download: Download full-size image

Fig. 7. Pseudo binary equilibrium phase diagram of the Cu10Sn-SS316L alloy.

3.4. Variation in mechanical properties

The tensile properties of different cross-section slices extracted from the CGA along the GD are assessed. It was noted that tensile specimens extracted from sections with 10–40 wt.% Cu10Sn fail prematurely before yield owing to the presence of cracks in them (see Fig. 3). Since the tensile data measured from these slices are unreliable and not representative of material properties, they were excluded from further analysis. Representative engineering stress, σ_E, vs engineering strain, ε_E, plots of cross-sections with 0, 50, 60, 70, 80, 90 and 100 wt.% Cu10Sn are shown in Fig. 8**(b)**. The yield strength, σy, ultimate tensile strength (UTS), elongation (ε_f) of all cross-sections are listed in Table 3. σ_y and UTS of the section with 50 wt.% Cu10Sn is ~691 and ~730 MPa, respectively. In sections with 60, 70 and 80 wt.%, σ_y decreases, but only marginally, to 654, 637 and 628 MPa, respectively. The variations in UTS are remain broadly invariant in the range of 787~800 MPa. However, σ_y and UTS reduce considerably to 541 and ~709 MPa in the section with 90 wt.% Cu10Sn.

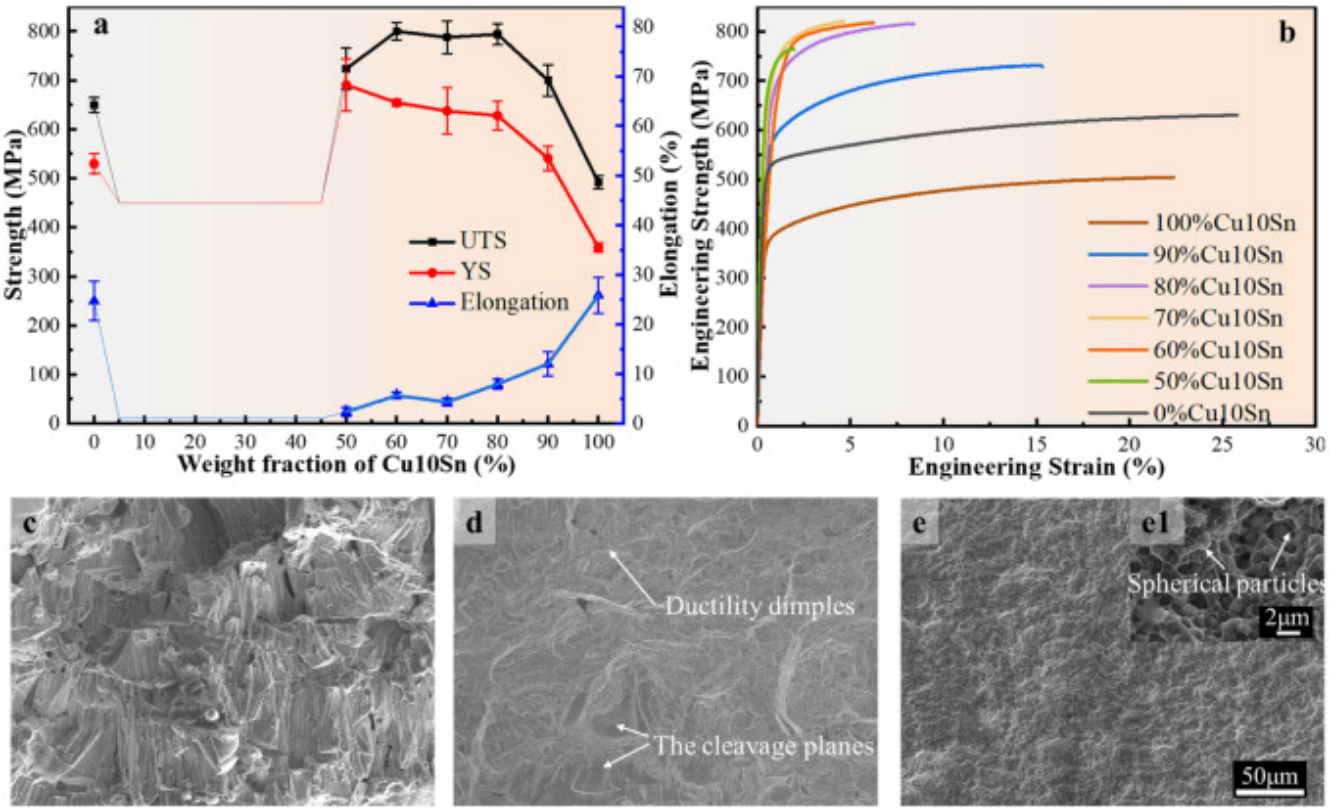

1. Download: Download high-res image (858KB)
2. Download: Download full-size image

Fig. 8. (a) variations of mechanical properties in the SS316L/Cu10Sn CGA along the GD. (b) representative engineering stress (σE) versus engineering strain (ε_E) curves of different cross-section slices of the CGA. Fracture surface of the tensile-tested sample extracted from cross-section with (c) 20, (d) 50 and (e) 80 wt.% Cu10Sn slices and (e1) at high magnification.

Table 3. Tensile properties, σ_y (yield strength), UTS (ultra-tensile strength), ε_f (elongation to failure), and *n* (strain hardening exponent), of different cross sections.

wt.% Cu10Sn	σ_y	**UTS**	ε_f	***n***
0	515±5	630±8	26±1.3	0.189
50	691 ± 13	730±3	2.9 ± 0.9	–
60	654 ± 6	800 ± 17	5.3 ± 0.7	0.077
70	637 ± 47	787 ± 33	4.5 ± 0.8	0.079
80	628 ± 29	794 ± 21	9.5 ± 0.9	0.105
90	541 ± 25	709 ± 21	13.1 ± 1.5	0.159
100	359 ± 9	492 ± 13	22.0 ± 3.6	0.216

Sections with 0 and 100 wt.% Cu10Sn have relatively lower σ_y of 520 and 359 MPa, UTS of 650 and 492 MPa, respectively. The variations in ε_f with increasing wt.% Cu10Sn contrast with those of σ_y and UTS. While the ε_f of the cross-section with 0 wt.% Cu10Sn is ~ 25 ± 0.2 %, it is only 2.9 ± 0.9 % in the section with 50 wt.% Cu10Sn. In cross sections with 60 and 70 wt.% Cu10Sn, ε_f increases to 5.7 ± 0.7 and 4.5 ± 0.7 %, respectively. With further increase in Cu10Sn content in the CGA, there is a monotonic increase in ε_f. For instance, ε_f ~9.5 and 13%, in sections with 80 and 90 wt.% Cu10Sn, respectively.

In the σ_E- ε_E plots of most cross-sections, it is observed that there is strain hardening after yielding. To understand the strain hardening behavior of different cross-sections, the portions of flow curves between σ_y and UTS are fitted with the power-law: $\sigma_T=K(\varepsilon_T)^n$, where K is a constant, σ_T is the true stress, and ε_T is the true strain. The values of *n* are listed in Table 3. Owing to limited post yielding deformation in the cross-section with 50 wt.% Cu10Sn, the accurate value of *n* from its flow curves could not be determined. Regardless, note that the variations of *n* with increasing Cu10Sn content in the CGA are similar to that of ε_f. Moreover, in all cross sections, except in the ones with 70 and 100 wt.% Cu10Sn, *n* is approximately ~ ε_f. The Considère's criterion for necking suggests that in tensile tests, the total uniform strain, ε_u, should be equal to the strain hardening exponent, *n*. Note that in the flow curves of most of the cross-section slices, there is no post-necking elongation, i.e., they fail immediately after the applied stress equals UTS. Therefore, ε_u, which is the strain measured up to UTS, is ~ ε_f, which in turn, based on Considère's criterion, is expected to be ~ *n* for most of the cross-sections of the CGA.

In Fig. 9, a plot of the variations of UTS with ε_f of the sections with 60, 70, 80, and 90 wt.% Cu10Sn in the CGA is displayed. For comparison, the values of UTS and εf of Cu-Fe alloys, Cu10Sn and SS316L, obtained from literature are also included in the plot. It is observed that the strength of only three Cu-Fe alloys reported in literature match or exceed the average UTS of SS316L. However, in terms of ductility, only half of them exhibits ε_f of ~5 %. In contrast, it is evident that not only do sections with 60, 70, 80, and 90 wt.% Cu10Sn have $\varepsilon_f \geq 5$ %, but also have significantly higher UTS than that of SS316L. In fact, the section with 80 wt.% Cu10Sn exhibits the best combination of high strength and good ductility (~10 %). Note that we considered εf ~5 % as the benchmark for ductility as some structural design standards consider ~5 % post yield plastic strain as a basic requirement for load bearing structural components [52], [53], [54]. Overall, compared to sections with 0 and 100 wt.% Cu10Sn, sections with 50–80 wt.% Cu10Sn have higher σ_y and UTS, but lower ductility. Also, in these sections, σ_y and UTS only changes by ~5–10 % with each 10 wt.% increase in Cu10Sn content, which implies that they are of similar strengths. In contrast, the ductility increases by 2 folds and 3 folds when the composition of the CGA increases from 50 to 60 wt.% Cu10Sn and 80 wt.% Cu10Sn, respectively. Nevertheless, sections with 0 and 100 wt.% Cu10Sn have the highest ductility of ≥ 25 %. On another note, while the ductility of the section with 90 wt.% Cu10Sn is 50 % lower than that of the section with 0 wt.% Cu10Sn, their σ_y and UTS are similar.

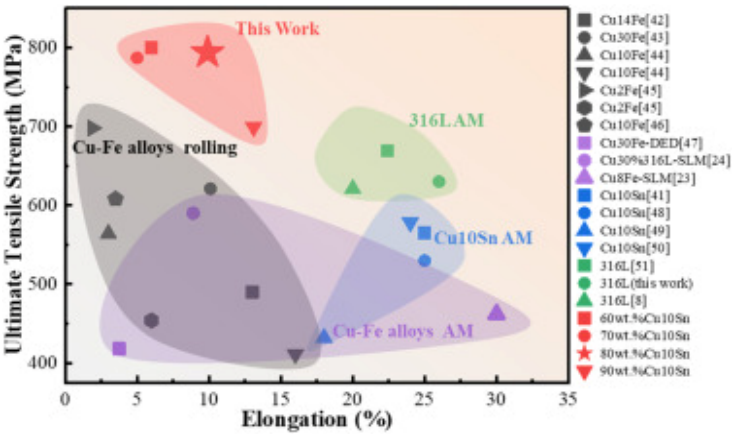

1. Download: Download high-res image (187KB)
2. Download: Download full-size image

Fig. 9. Ultimate tensile strength versus elongation of this as compared with 316 L alloy and Cu10Sn alloys produced by AM methods, and Cu-Fe alloys produced by AM methods and conventional technologies [8,23,24,[41], [42], [43], [44], [45], [46], [47], [48], [49], [50], [51]].

Fig. 8**(c)–(e)** display the fracture surfaces of tensile-tested samples that were extracted from cross sections with 20, 50 and 80 wt.% Cu10Sn (fractography of other cross-sections are shown in **Figs. S6 and S7**). In the section with 20 wt.% Cu10Sn, which is representative of fracture surfaces in sections with 10–40 wt.% Cu10Sn, shown in Fig. 8**(c)**, the fracture surface exhibits both rough and flat features, which are indicative of brittle fracture. Since the tensile samples from these cross-sections (10–40 wt.% Cu10Sn) failed before yielding, brittle fracture features are expected. For the section with 50 wt.% Cu10Sn, both cleavage and dimples were observed on the fracture surface. These features suggest that the failure mechanism is a mix of ductile and brittle fracture. The fracture surface of the section with 80 wt.% Cu10Sn, shown in Fig. 8**e**, contains uniform fine dimpled features, within which several nano-scale and sub-micron sized spherical phases are embedded. Note that the average sizes of these micron sized and nano-scale phases match with that of the spherical α-Fe phase embedded within the α-Cu matrix in the CGA (see Fig. 4).

4. Discussion

4.1. Microstructure formation mechanism of the Cu10Sn-SS316L CGA

During LPBF, the laser melts an alloy powder within mesoscale sized 'melt pools' from which heat is extracted via the surrounding un-melted alloy powders and the substrate. As a result, there is directional solidification of the molten alloy, which initiates at the melt pool boundaries. In the case of unmixed alloy powders, directional solidification leads to the formation of columnar or dendritic grains whose axes are parallel to BD. This explains the observed formation of columnar and dendritic grains in cross sections of the CGA with 0 and 100 wt.% Cu10Sn (see **Fig. S3**). A similar microstructure is obtained when two pre-alloyed powders of different compositions are mixed and processed by LPBF, if they exhibit good solid and liquid miscibility. For instance, in all cross-section slices of IN718/SS316L and IN718/CoCrMo CGAs, columnar grains were observed as the constituent alloys exhibit good liquid and solid-state miscibility. Most constituent elements of the alloys employed in this study, SS316L and Cu10Sn, with the exception of Cu and Ni, have a positive enthalpy of mixing [10]. Therefore, the two alloys, when mixed in certain proportions, will exhibit a miscibility gap in the molten state, which was observed in the phase diagram shown in Fig. 7. The two alloys remain immiscible even in the solid state, which leads to the formation of hierarchical microstructures containing micron-scale γ-Fe grains and nanoscale α-Cu and α-Fe grains on solidification in the CGA.

To understand the formation mechanism and evolution along the composition gradient of the microstructure, phase-field simulations coupled with linearized pseudo-binary phase diagrams were conducted for different sections of the CGA. Such simplified phase diagrams for sections with 20, 40, 60 and 80 wt.% Cu are shown in **Fig. S10**(a) and (b). Based on these linearized phase diagram, the phase-field simulated microstructure evolution for the 4 sections of the CGA at melt pool scale during solidification is shown in Fig. 10. During LPBF in all the sections of the CGA, the powders of Cu10Sn and SS316L melt and form a homogeneous liquid solution, *L*. In the slice with 20 wt.% Cu, which is representative of slices with 10–20 wt.% Cu10Sn, at ~1610 K, solid γ-Fe nucleates within the melt, but the remaining liquid remains rich in SS316L, and is hence referred to as *L*-Fe (see Figs. 10**(a1) and S10(a)**). Concurrently, Cu, owing to its poor solubility in γ-Fe is expelled to *L*-Fe. Since Cu has limited solubility in *L*-Fe as well, the liquid near the boundaries of γ-Fe, which is enriched in Cu, forms thin bands of *L*-Cu (see Fig. 10**(a2)**). Therefore, the continuous growth of γ-Fe with further cooling facilitates the phase separation or spinodal decomposition of *L*-Cu and *L*-Fe. When the temperature drops further, all the *L*-Fe transforms to γ-Fe and the microstructure consists of γ-Fe grains surrounded by thin bands of *L*-Cu (see Fig. 10**(a3)**). In cross-sections with 40 wt.% Cu, which is representative slice with 30–50 wt.% Cu-10Sn, the liquid undergoes spinodal decomposition at 1653 K and small islands of *L*-Cu form inside *L*-Fe (see Figs. 10**(b1) and S10(a)**). The composition profile of the *L*-Cu nuclei is non-uniform, i.e., the interior is rich in Cu whereas the surface layer is rich in Fe. This fact is attributed to the expulsion of Fe from the interior of *L*-Cu. With further cooling, the *L*-Cu islands undergo limited growth, and the nucleation of γ-Fe begins. Note that γ-Fe nucleates preferentially from the regions surrounding *L*-Cu islands as the Fe concentration is locally higher at the locations (see Fig. 10**(b2)**). Further cooling leads to the growth of the γ-Fe phase and

islands of *L*-Cu (see Fig. 10**(b3)**). In contrast, while the same sequence of phase transformations is observed in the cross-sections with 60 and 80 wt.% Cu10Sn, their microstructures evolve differently. In these cross-sections, since the relative content of SS316L is lower than that of Cu10Sn, several large islands of *L*-Cu form in *L*-Fe, which has significant Cu content (see Fig. 10**(c1) and (d1)**). These islands of *L*-Cu grow significantly in size and fuse together as Cu is expelled from *L*-Fe (see Fig. 10**(d2)**). In fact, the islands of *L*-Cu fuse together to the extent that it becomes a continuous matrix, wherein pockets of *L*-Fe are present (see Fig. 10(**d3)**). Finally, in both slices, γ-Fe grains form within the pockets of *L*-Fe. On complete solidification, *L*-Fe and the large islands of *L*-Cu fully transform to micron sized γ-Fe and α-Cu grains, respectively. However, it should be noted that in all the sections, a thin band of *L*, which contains Fe and Cu in similar proportions, surrounds the *L*-Cu phase.

w(Cu)=20wt.%
w(Cu)=40wt.%
w(Cu)=60wt.%
w(Cu)=80wt.%
(a1)
L-Fe
γ-Fe
1.8 s
(a2)
2.2 s
(a3)
L-Cu
2.8 s
20μm
(b1)
L-Fe
1.0 s
L-Cu
(b2)
1.8 s
(b3)
γ-Fe
2.8 s
20μm
(c1)
L-Fe
L-Cu
2.0 s
(c2)
4.5 s
(c3)
γ-Fe
6.0 s
20μm
(d1)
L-Cu
L-Fe
2.0 s
(d2)
4.1 s
(d3)
γ-Fe
4.4 s
20μm

1. Download: Download high-res image (2MB)
2. Download: Download full-size image

Fig. 10. Snapshots of the phase-field simulated microstructure at different times for Cu-Fe mixtures with, (a1)–(a3) w(Cu)=20 wt.%, (b1)–(b3) w(Cu)=40 wt.%, (c1)-(c3) w(Cu)=60 wt.% (d1)–(d3) w(Cu)=80 wt.%.

To understand the phase evolution of the *L-Cu* on cooling, the phase-field simulation results in nanoscale are presented in Fig. 11. The initial composition of the residual liquid phase, w(Cu)=84 wt.%, is generated from the average composition of the L-Cu phase in Fig. 10**(a3 ~ d3)**. The entire solidification process in the bands occurs in four stages. In the first stage, α-Cu, which contains ~97 wt.% Cu, preferentially nucleates and grows in *L*, which has ~84 wt.% Cu (see Fig. 11**(a)**). The second stage involves the expulsion of Fe from α-Cu owing to its low solubility, which in turn, elevates its concentration in the vicinity of the latter and facilitates the formation of γ-Fe in *L* in the proximity of α-Cu (see Fig. 11**(b))**. To consider the possibility that α-Cu is a heterogeneous nucleation site for γ-Fe, we calculated the interface energy of γ-Fe/α-Cu and compared it with that of Liquid/γ-Fe and Liquid/α-Cu interfaces. Since interface energies of γ-Fe/α-Cu and Liquid/γ-Fe and Liquid/α-Cu is 0.62 J/m^2, 0.30 J/m^2 and 0.10 J/m^2 [55], [56], [57], respectively, it was concluded that α-Cu is not a preferred heterogeneous nucleation site for γ-Fe. Alternately, spherical precipitates of γ-Fe form as a consequence of a strong curvature contribution to its chemical potential. Finally, as shown in Fig. 11**(d)**, the microstructure evolves as a fine dispersion of γ-Fe nanospheres in the matrix of α-Cu. The simulation results match well with the microstructural morphology observed in experiments (see Fig. 4). It is also evident that while there are several γ-Fe precipitates, they undergo limited growth. This fact is attributed to the large degree of undercooling during spinodal decomposition of *L* in the temperature range of 1665.15–1375.15 K, which facilitates higher nucleation rate at the expense of growth. The propensity for nucleation is further amplified by the high cooling rate within the melt-pool in LPBF. Finally, based on the linearized phase diagrams, when the temperature is below 870 K, the γ-Fe precipitates transform to α-Fe.

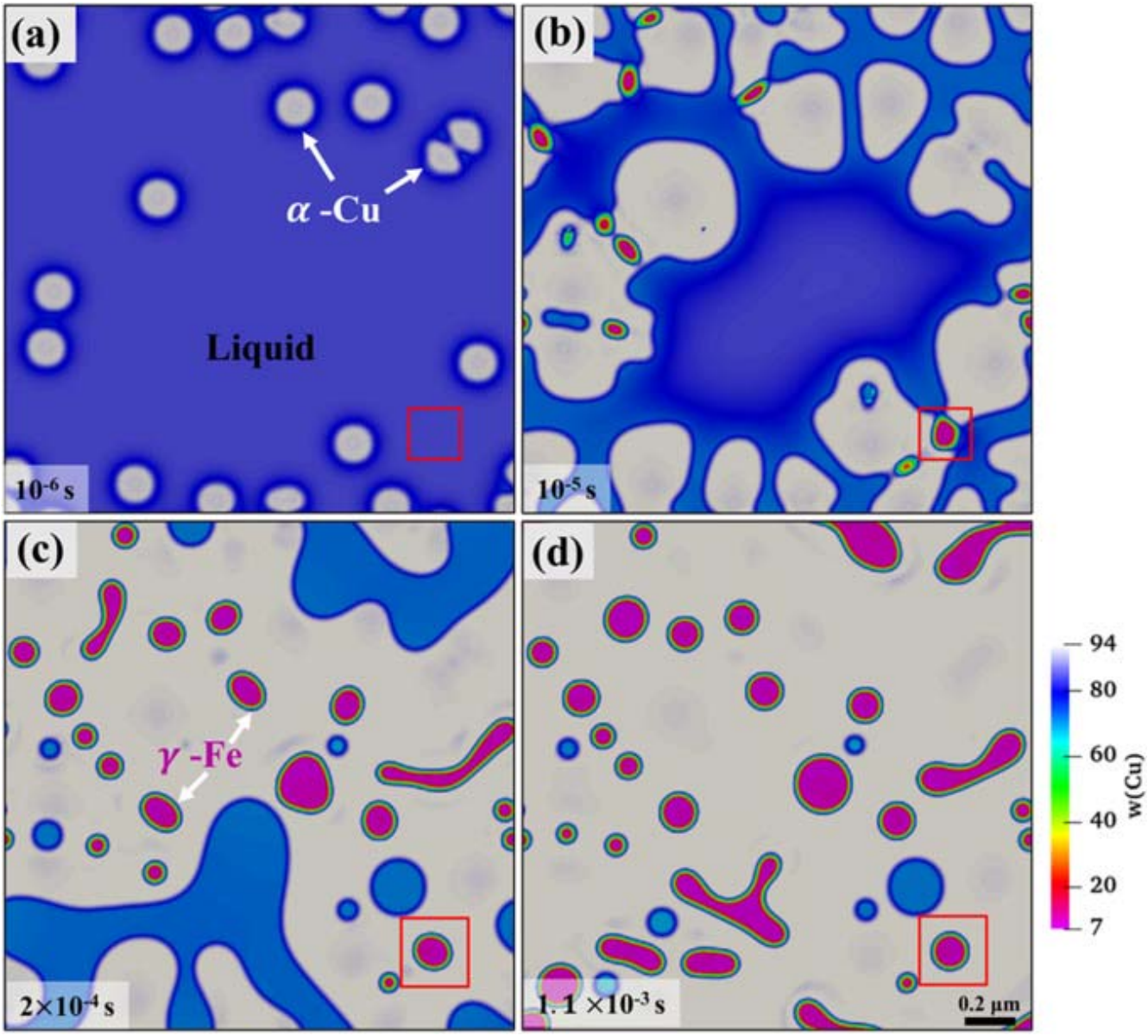

1. Download: Download high-res image (1MB)
2. Download: Download full-size image

Fig. 11. Snapshots of the phase-field simulated microstructure within *L-Cu* in the Cu-Fe mixture with w(Cu)=80 wt.% of the CGA at (a) 10^{-6} s, (b) 10^{-5} s, (c) 2×10^{-4} s and (d) 1.1×10^{-3} s. (see Fig. 10(d3)).

One may also enquire as to why the solidified spherical droplets of γ-Fe in nano scale, which are embedded in the L_{Cu}, undergo transformation to α-Fe at 870 K in cross-sections with 10–90 wt.% Cu10Sn whereas some of the columnar γ-Fe in micron scale grains do not. To answer this question, further EDS spot analysis of the α-Fe and γ-Fe grains present in the cross-section with 60 wt.% Cu10Sn is performed at four points, labelled points 1, 2, 3 and 4, and the results are displayed in **Fig. S8 and Table S2**. Points 1 and 2 correspond to the composition of α-Fe, whereas points 3 and 4 correspond to the composition of γ-Fe. Similarly, spot analysis of spherical nanoscale α-Fe and α-Cu

precipitates is shown in **Fig. S9 and Table S3**. In this case, points 1 and 2 are locations within the α-Fe and α-Cu phase, respectively. Note that the ratio of Fe/Ni in α-Fe is > 10, whereas that in γ-Fe ~ 7. In contrast, the ratio of Fe/Cr is ~5 in both phases. In contrast, α-Cu is lean in alloying elements and contains only 2 at.% and < 1 at.% of Ni and Cr, respectively. While α is the equilibrium room temperature stable phase of Fe, a high Ni content in it is expected to stabilize the high temperature γ phase. Therefore, there will be relatively higher Ni content within the grains and its lower content within the solid spherical droplets (and some columnar grains). This explains why they exist as the γ-Fe and α-Fe at room temperature. Here, it must be recognized that Ni has a higher affinity to bind with Cu than with Fe, owing to the relatively lower mixing enthalpy of Ni and Cu [10]. It is therefore expected that the nanoscale γ-Fe precipitates within the α-Cu matrix get significantly more enriched in Ni and Cr, which triggers its massive transformation to α-Fe below 870 K.

We next address the formation of cracks in cross-sections with 10–40 wt.% Cu10Sn at the γ-Fe grain boundaries. The solidification cracking of the as-printed alloys can be measured by crack susceptibility index, CSI (see Eq. (1)). A high CSI value indicates that there should be a longer intergranular passageway and slower lateral growth of two neighboring grains, which lead to lower extend of liquid feeding and hence a higher susceptibility to cracking. Based on the high-throughput Scheil-Gulliver simulations, the CSI of all cross-sections of CGA are displayed in Fig. 12. In cross sections with 0–5 wt.% Cu10Sn and that with > 90 wt.% Cu10Sn, CSI is $\langle 10^4$. However, in the slice with ~ 5 wt.% Cu10Sn CSI increases sharply and reaches a peak value of 1.11×10^6. CSI decreases gradually with increasing Cu10Sn content in the CGA but remains $\rangle\ 10^4$. However, at cross sections with 50 wt.% Cu10Sn, CSI again dramatically increases to 3.97×10^4. The higher cracking tendency of cross-sections with 5~50 wt.% Cu10Sn, which is also observed in experiments (see **Fig. S2)**, is attributed to the dendritic solidification of γ-Fe along the thermal gradient, which provides too narrow a intergranular channel for *L*-Cu to flow and accommodate solidification shrinkage. In sections with > 50 wt.% of Cu10Sn in the CGA, CSI decreases monotonically to values < 10^4, with the exception of the section with 70 wt.% Cu10Sn, where CSI is ~ 9317.89. The broadly lower cracking tendency of these sections is the outcome of the significant increase in the content of *L*-Cu, which interrupts the dendritic growth of γ-Fe grains and prevents solidification cracking.

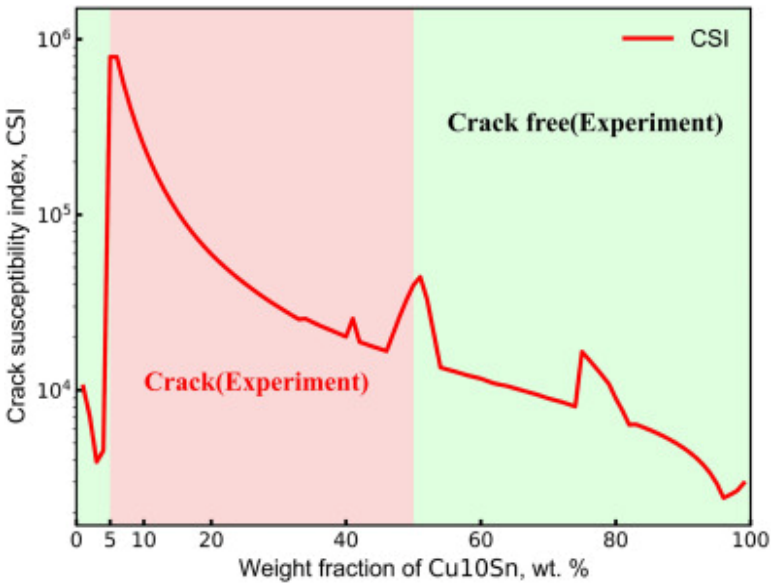

1. Download: Download high-res image (190KB)
2. Download: Download full-size image

Fig. 12. Variations of the calculated crack susceptibility index (CSI) for the Cu10Sn-SS316L CGA based on Scheil-Gulliver solidification simulations.

4.2. Strengthening mechanisms and other considerations

Cross-sections with 50–90 wt.% Cu10Sn in the CGA exhibit considerable strengthening compared to their individual components (i.e., cross-sections with 100 wt.% SS316L and 100 wt.% Cu10Sn) when processed via LPBF. Fig. 13**(a)** displays the bright field TEM image of the tensile-tested sample extracted from the cross-section slice with 80 wt.% Cu10Sn. In between the spherical α-Fe phases, several clusters of curved black lines, identified as dislocations (marked with yellow arrows) were observed in the α-Cu matrix. Since the microstructure and YS of the cross-sections with 50–90 wt.% are similar, the operative strengthening mechanisms in them are also expected to be broadly the same. At the outset, the primary contributor to elevated YS of these cross-sections is grain boundary strengthening as the grains in them are significantly more refined than those in the cross-sections with 100 wt.% SS316L and 100 wt.% Cu10Sn. Besides this, particulate strengthening is provided by the sub-micron scale solid spherical α-Fe droplets embedded in the α-Cu matrix. Grain boundary strengthening, $\Delta\sigma_{HP}$, is calculated from the Hall-Petch relationship [58],

$$\Delta\sigma_{HP} = k_{HP} \cdot d^{-\frac{1}{2}} \tag{9}$$

where k_{HP}~3379 MPa/nm$^{-1/2}$ is the Hall-Petch coefficient and d is the average grain size. Similarly, since α-Fe spherical particles share an incoherent interface with α-Cu matrix, particulate strengthening, $\Delta\sigma_{PS}$, is mediated by Orowan bypass mechanism, where the dislocations loop around the particles. An estimate of $\Delta\sigma_{PS}$ is obtained from,

$$\Delta\sigma_{PS} = M\frac{0.4Gb}{\pi\sqrt{1-\upsilon}}\frac{\ln(2r/b)}{L} \quad (10)$$

and

$$L = \sqrt{\frac{8}{3}}r\left(\sqrt{\frac{\pi}{4f}} - 1\right) \quad (11)$$

is the Taylor factor of FCC structure, υ ~0.35 is the Poisson's ratio of the alloy, L ~160 nm is the mean α-Fe particle spacing, G ~48 GPa is the shear modulus of Cu, b ~0.25 nm is the Burgers vector in α-Cu, r ~80 nm is the mean α-Fe precipitate radius and f is the volume fraction of spherical particles. For the ~80 wt.% Cu10Sn slice, where there are few γ-Fe grains, the calculated strengthening contributions of the grain boundary and Orowan bypass are 127 MPa and 233 MPa, respectively. By considering the weighted average of the two microstructural components, γ-Fe grains and α-Fe embedded in α-Cu matrix, similar calculations can be performed for other sections as well. Note that since the α-Cu matrix is lean in other constituents (see **Table S3**), the solid solution strengthening is not expected to be significant. Post yielding, the cross-sections with 50–90 wt.% Cu10Sn exhibit varying degrees of plastic deformation and strain hardening.

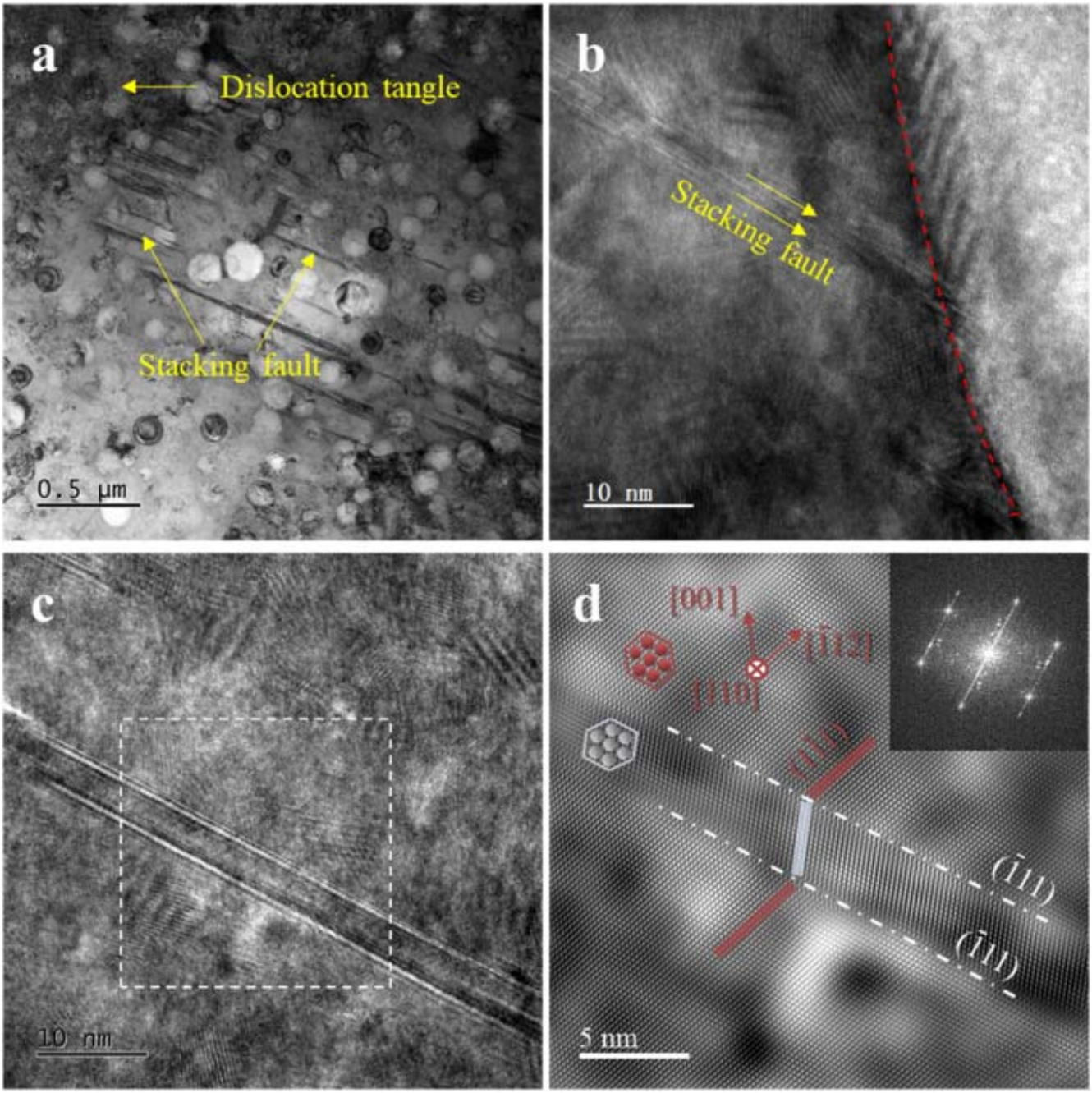

1. Download: Download high-res image (2MB)
2. Download: Download full-size image

Fig. 13. (a) Bright field TEM image of the side surfaces extracted from the tensile-tested specimen with 80 wt.% Cu10Sn. HRTEM images of (b) the interface between α-Cu and α-Fe, and (c) a stacking fault in the matrix, while (d) FFT and IFFT images of the stacking fault in (c).

However, while these sections strain harden beyond yield, their strain hardening rate and the ductility are at least 50 % lower than those of cross-sections with 100 wt.% SS316L and 100 wt.% Cu10Sn (see Table 3). Note that in the HRTEM images of the side surfaces

extracted from the tensile-tested specimen with 80 wt.% Cu10Sn, several black streaks were observed in the α-Cu matrix that terminate at the α-Fe phase-matrix interface and another that terminates within the matrix (see Fig. 13**(a)–(c)**). The fast Fourier transform (FFT) pattern and inverse fast Fourier transform (IFFT) pattern of the streak, shown in Fig. 13**(d)**, reveals that it is a stacking fault. Note that most of the spherical particles remain undistorted post deformation implying that they act as obstacles to dislocation motion (leading to the Orowan looping) and stacking faults. The FFT patterns indicate that the stacking faults form on the {111} FCC Cu planes and their nucleation is triggered by the homogeneous shear of the Shockley partials on {111} planes. The dislocation dissociation reaction leading to this stacking fault is, $a/2[110] = a/6[121] + a/6[2\bar{1}1]$, where a is the lattice constant of α-Cu [59]. We believe that this is the outcome of the increased Ni content in the α-Cu matrix, which lowers its stacking fault energy. The lower stacking fault energy of α-Cu promotes the formation of several stacking faults in it during deformation (see Fig. 13). Note that these stacking faults are bounded by partial dislocations, which are inherently sessile. Moreover, the partials on different (111) planes can interact and form the Lomer-Cottrell locks or 'stair-rod' dislocations. These locks induce slip planarity by mitigating cross-slip of dislocations, which are otherwise necessary for strain hardening. Consequently, the cross-sections with 50–80 wt.% Cu10Sn exhibit lower strain hardening than the cross-section with 100 wt.% Cu10Sn.

Regardless, it is evident that in the LPBF processed CGA of Cu10Sn-SS316L alloy, cross-sections with 50–80 wt.% of Cu10Sn have excellent strength and reasonably good ductility. Alternately, when Cu10Sn and SS316L are processed together–in any proportion–via casting and other conventional processing methods, liquation cracks form in the material, which compromises its mechanical properties [60,61]. This implies that the hierarchical microstructural features inherited by the sections in the CGA, during LPBF processing plays a key role in ensuring synergistic enhancement in strength and ductility. In addition, in the LPBF processed alloys, repeated runs of the laser over several layers of the build increases the temperature of the build, which can potentially drive grain growth of the α-Cu matrix. There is a possibility that such grain growth will diminish the Hall-Petch strengthening effect in the matrix. However, the solidified spherical α-Fe droplets present in the matrix pin the grain boundaries (via the Zener pinning mechanism) [62] and prevent grain growth of the α-Cu grains.

Before closing, it is worth identifying the ideal proportions of Cu10Sn and SS316L that can be mixed together for the LPBF processing. Any build made from an alloy mixture that has 10–40 wt.% Cu10Sn is not suitable for structural applications. Alternately, while those with 50–90 wt.% Cu10Sn possess good ductility, only the cross-section with 80 wt.% Cu10Sn has the optimum combination of strength and ductility.

5. Conclusions

Using a customized LPBF process that creates a compositional gradient along the powder bed plane, a CGA of two immiscible alloys, SS316L and bronze (Cu10Sn) is fabricated in this study. The composition resolution and dimensions of the CGA are sufficient to assess

the printability and perform a study on the structure-mechanical property correlations as a function of composition. The key findings of this study are summarized as follows:

1) The microstructure of the cross-sections with 0–50 wt.% Cu10Sn predominantly contains micron sized columnar grains of γ-Fe. With an increase in content of Cu10Sn, the grain boundaries are filled with equiaxed and submicron sized α-Cu grains that also have nanoscale α-Fe particles embedded within them. Sections with 50–100 wt.% Cu10Sn predominantly consist of a α-Cu matrix, with embedded α-Fe particles, and a few γ-Fe grains. Only cross-sections with 10–40 wt.% Cu10Sn undergo solidification cracking and contain numerous pores owing to restricted liquid feeding in interdendritic areas of γ-Fe, whereas other sections are reasonably dense and crack-free.
2) Phase field simulations suggest that the formation of these hierarchical microstructures in different sections is the consequence of multiple phase transformations in the micron and nanoscale, which is supplemented by the ultrafast cooling rate within the small melt-pools of metal in LPBF. In the micron scale, liquid decomposition ($L \rightarrow L$-Fe+L-Cu) and the solidification of primary γ-Fe grains occurs simultaneously. Alternately, in the nano scale, γ-Fe nuclei form within the solute lean α-Cu and later undergo massive transformation to α-Fe.
3) Owing to presence of cracks in cross-sections with 10–40 wt.% Cu10Sn, their YS, UTS and ductility could not be reliably measured from tension tests. The cross-sections with 50–80 wt.% Cu10Sn, have superior YS and UTS than those with 0 and 100 wt.% Cu10Sn but lower ductility. The significant enhancement in strength is attributed to grain refinement of α-Cu and precipitate strengthening from dislocation looping around α-Fe particles.
4) The results and observations from this investigation can be generalized for developing alloys of immiscible alloys using LPBF.

Declaration of Competing Interest

The authors declare that they have no known competing financial interests or personal relationships that could have appeared to influence the work reported in this paper.

Acknowledgments

The authors acknowledge the National Natural Science Foundation of China (Nos.: 52171026), Start-up research grant (No. SRG/2020/000095) of Science and Engineering Research Board, DST, GoI. A*STAR, Singapore via the Structural Metals and Alloys Program (No. A18B1b0061). The computing work is supported by USTB MatCom of Beijing Advanced Innovation Center for Materials Genome Engineering.

Appendix. Supplementary materials

Download: Download Word document (11MB)

References

[1]

S. Chen, J. Huang, J. Xia, H. Zhang, X. Zhao

Microstructural characteristics of a stainless steel/copper dissimilar joint made by laser welding

Metall. Mater. Trans. A Phys. Metall. Mater. Sci., 44 (2013), pp. 3690-3696, 10.1007/S11661-013-1693-Z/FIGURES/9
View in ScopusGoogle Scholar
[2]

Y. Xu, X. Hou, Y. Shi, W. Zhang, Y. Gu, C. Feng, K. Volodymyr

Correlation between the microstructure and corrosion behaviour of copper/316L stainless-steel dissimilar-metal welded joints

Corros. Sci., 191 (2021), Article 109729, 10.1016/j.corsci.2021.109729
View PDFView articleView in ScopusGoogle Scholar
[3]

H.D. Vyas, K.P. Mehta, V. Badheka, B. Doshi

Microstructure evolution and mechanical properties of continuous drive friction welded dissimilar copper-stainless steel pipe joints

Mater. Sci. Eng. A, 832 (2022), Article 142444, 10.1016/J.MSEA.2021.142444
View PDFView articleView in ScopusGoogle Scholar
[4]

N. Switzner, H. Queiroz, J. Duerst, Z. Yu

Si-bronze to 304 stainless steel GTA weld fusion zone microstructure and mechanical properties

Mater. Sci. Eng. A, 709 (2018), pp. 55-64, 10.1016/J.MSEA.2017.09.025
View PDFView articleView in ScopusGoogle Scholar
[5]

D.W. Lee, Y.D. Bae, S.K. Kim, B.G. Hong, J.H. Lee, J.Y. Park, Y.H. Jeong , B.K. Choi

High heat flux test with HIP-bonded Cu/SS mock-ups for the ITER first wall

Fusion Eng. Des., 83 (2008), pp. 1038-1043, 10.1016/J.FUSENGDES.2008.08.023
View PDFView articleView in ScopusGoogle Scholar
[6]

Y. Liu, J. Zhang, Q. Tan, Y. Yin, S. Liu, M. Li, M. Li, Q. Liu, Y. Zhou, T. Wu , F. Wang, M.X. Zhang

Additive manufacturing of high strength copper alloy with heterogeneous grain structure through laser powder bed fusion

Acta Mater., 220 (2021), Article 117311, 10.1016/j.actamat.2021.117311
View PDFView articleView in ScopusGoogle Scholar
[7]

S. Qu, J. Ding, J. Fu, M. Fu, B. Zhang, X. Song

High-precision laser powder bed fusion processing of pure copper

Addit. Manuf., 48 (2021), Article 102417, 10.1016/j.addma.2021.102417
View PDFView articleView in ScopusGoogle Scholar
[8]

P. Kumar, R. Jayaraj, J. Suryawanshi, U.R. Satwik, J. McKinnell, U. Rama murty

Fatigue strength of additively manufactured 316L austenitic stainless steel

Acta Mater., 199 (2020), pp. 225-239, 10.1016/j.actamat.2020.08.033
View PDFView articleGoogle Scholar
[9]

I. Sen, E. Amankwah, N.S. Kumar, E. Fleury, K. Oh-ishi, K. Hono, U. Ramamurty

Microstructure and mechanical properties of annealed SUS 304H austenitic stainless steel with copper

Mater. Sci. Eng. A, 528 (2011), pp. 4491-4499, 10.1016/J.MSEA.2011.02.019
View PDFView articleView in ScopusGoogle Scholar
[10]

A. Takeuchi, A. Inoue

Mixing enthalpy of liquid phase calculated by miedema's scheme and approximated with sub-regular solution model for assessing forming ability of amorphous and glassy alloys

Intermetallics, 18 (2010), pp. 1779-1789, 10.1016/j.intermet.2010.06.003
View PDFView articleView in ScopusGoogle Scholar
[11]

T. Soysal, S. Kou, D. Tat, T. Pasang

Macrosegregation in dissimilar-metal fusion welding

Acta Mater., 110 (2016), pp. 149-160, 10.1016/j.actamat.2016.03.004
View PDFView articleView in ScopusGoogle Scholar
[12]

L. Ratke, S. Diefenbach

Liquid immiscible alloys

Mater. Sci. Eng. R, 15 (1995), pp. 263-347, 10.1016/0927-796X(95)00180-8
View PDFView articleView in ScopusGoogle Scholar
[13]

E. Ma

Alloys created between immiscible elements

Prog. Mater. Sci., 50 (2005), pp. 413-509, 10.1016/J.PMATSCI.2004.07.001
View PDFView articleView in ScopusGoogle Scholar
[14]

J. Zhao, H. Jiang

Progress in the solidification of monotectic alloys

Jinshu Xuebao Acta Metall. Sin., 54 (2018), pp. 682-700, 10.11900/0412.1961.2018.00080
Google Scholar
[15]

R.P. Shi, C.P. Wang, D. Wheeler, X.J. Liu, Y. Wang

Formation mechanisms of self-organized core/shell and core/shell/corona microstructures in liquid droplets of immiscible alloys

Acta Mater., 61 (2013), pp. 1229-1243, 10.1016/J.ACTAMAT.2012.10.033
View PDFView articleView in ScopusGoogle Scholar
[16]

J. He, J.Z. Zhao, L. Ratke

Solidification microstructure and dynamics of metastable phase transformation in undercooled liquid Cu-Fe alloys

Acta Mater., 54 (2006), pp. 1749-1757, 10.1016/j.actamat.2005.12.023
View PDFView articleView in ScopusGoogle Scholar
[17]

C.P. Wang, X.J. Liu, I. Ohnuma, R. Kainuma, K. Ishida

Formation of immiscible alloy powders with egg-type microstructure

Science, 297 (2002), pp. 990-993, 10.1126/science.1073050
View in ScopusGoogle Scholar
[18]

D. Favez, L. Deillon, J.D. Wagnire, M. Rappaz

Intergranular penetration of liquid gold into stainless steel

Acta Mater., 59 (2011), pp. 6530-6537, 10.1016/J.ACTAMAT.2011.06.030
View PDFView articleView in ScopusGoogle Scholar
[19]

J.E. Norkett, M.D. Dickey, V.M. Miller

A review of liquid metal embrittlement: cracking open the disparate mechanisms

Metall. Mater. Trans. A Phys. Metall. Mater. Sci., 52 (2021), pp. 2158-2172, 10.1007/s11661-021-06256-y
View in ScopusGoogle Scholar
[20]

J. Li, Y. Cai, F. Yan, C. Wang, Z. Zhu, C. Hu

Porosity and liquation cracking of dissimilar Nd:YAG laser welding of SUS304 stainless steel to T2 copper

Opt. Laser Technol., 122 (2020), Article 105881, 10.1016/J.OPTLASTEC.2019.105881
View PDFView articleView in ScopusGoogle Scholar
[21]

A. Zafari, K. Xia

Laser powder bed fusion of ultrahigh strength Fe-Cu alloys using elemental powders

Addit. Manuf., 47 (2021), Article 102270, 10.1016/j.addma.2021.102270
View PDFView articleView in ScopusGoogle Scholar
[22]

A. Zafari, K. Xia

Nano/ultrafine grained immiscible Fe-Cu alloy with ultrahigh strength produced by selective laser melting

Mater. Res. Lett., 9 (2021), pp. 247-254, 10.1080/21663831.2021.1884620
View in ScopusGoogle Scholar
[23]

Y. Liu, J. Zhang, Q. Sun, M. Li, M. Yan, X. Cheng, M. Li, M.X. Zhang

Laser powder bed fusion of copper matrix iron particle reinforced nanocomposite with high strength and high conductivity

J. Mater. Sci. Technol., 134 (2023), pp. 50-59, 10.1016/J.JMST.2022.06.007
View PDFView articleGoogle Scholar
[24]

S. Zhou, M. Xie, C. Wu, Y. Yi, D. Chen, L.C. Zhang

Selective laser melting of bulk immiscible alloy with enhanced strength: heterogeneous microstructure and deformation mechanisms

J. Mater. Sci. Technol., 104 (2022), pp. 81-87, 10.1016/j.jmst.2021.06.062
View PDFView articleGoogle Scholar
[25]

D. Wang, G. wei Deng, Y. qiang Yang, J. Chen, W. hui Wu, H. liang Wang, C. Lin Tan

Interface microstructure and mechanical properties of selective laser melted multilayer functionally graded materials

J. Cent. South Univ., 28 (2021), pp. 1155-1169, 10.1007/s11771-021-4687-9
View in ScopusGoogle Scholar
[26]

L.D. Bobbio, R.A. Otis, J.P. Borgonia, R.P. Dillon, A.A. Shapiro, Z.K. Liu, A.M. Beese

Additive manufacturing of a functionally graded material from Ti-6Al-4V to Invar: experimental characterization and thermodynamic calculations

Acta Mater., 127 (2017), pp. 133-142, 10.1016/j.actamat.2016.12.070
View PDFView articleView in ScopusGoogle Scholar
[27]

B.E. Carroll, R.A. Otis, J.P. Borgonia, J. Suh, R.P. Dillon, A.A. Shapiro, D. C. Hofmann, Z.K. Liu, A.M. Beese

Functionally graded material of 304L stainless steel and inconel 625 fabricated by directed energy deposition: characterization and thermodynamic modeling

Acta Mater., 108 (2016), pp. 46-54, 10.1016/j.actamat.2016.02.019
View PDFView articleView in ScopusGoogle Scholar
[28]

Y. Wen, B. Zhang, R.L. Narayan, P. Wang, X. Song, H. Zhao, U. Ramamu rty, X. Qu

Laser powder bed fusion of compositionally graded CoCrMo-Inconel 718

Addit. Manuf., 40 (2021), Article 101926, 10.1016/j.addma.2021.101926
View PDFView articleView in ScopusGoogle Scholar
[29]

Y. Wen, J. Gao, R.L. Narayan, P. Wang, L. Zhang, B. Zhang, U. Ramamur ty, X. Qu

Microstructure-property correlations in as-built and heat-treated compositionally graded stainless steel 316L-Inconel 718 alloy fabricated by laser powder bed fusion

Mater. Sci. Eng. A, 862 (2023), Article 144515, 10.1016/j.msea.2022.144515
View PDFView articleView in ScopusGoogle Scholar
[30]

S. Kou

A criterion for cracking during solidification

Acta Mater., 88 (2015), pp. 366-374, 10.1016/J.ACTAMAT.2015.01.034
View PDFView articleView in ScopusGoogle Scholar
[31]

ASTM E3-11

Standard Guide for Preparation of Metallographic Specimens

ASTM International, West Conshohocken, PA (2011), 10.1520/E0003-11 (n.d.)
Google Scholar
[32]

ASTM E8

ASTM E8/E8M standard test methods for tension testing of metallic materials 1

Annu. B. ASTM Stand., 4 (2010), pp. 1-27, 10.1520/E0008
Google Scholar
[33]

Z. Lu, L. Zhang

Thermodynamic description of the quaternary Al-Si-Mg-Sc system and its application to the design of novel Sc-additional A356 alloys

Mater. Des., 116 (2017), pp. 427-437, 10.1016/j.matdes.2016.12.034
View PDFView articleView in ScopusGoogle Scholar
[34]

J. Zhang, J. Gao, B. Song, L. Zhang, C. Han, C. Cai, K. Zhou, Y. Shi

A novel crack-free Ti-modified Al-Cu-Mg alloy designed for selective laser melting

Addit. Manuf., 38 (2021), Article 101829, 10.1016/j.addma.2020.101829
View PDFView articleView in ScopusGoogle Scholar

[35]

J. Liu, S. Kou

Effect of diffusion on susceptibility to cracking during solidification

Acta Mater., 100 (2015), pp. 359-368, 10.1016/j.actamat.2015.08.064
View PDFView articleView in ScopusGoogle Scholar
[36]

I. Steinbach, F. Pezzolla, B. Nestler, M. Seeßelberg, R. Prieler, G.J. Schmitz, J.L.L. Rezende

A phase field concept for multiphase systems

Phys. D Nonlinear Phenom., 94 (1996), pp. 135-147, 10.1016/0167-2789(95)00298-7
View PDFView articleView in ScopusGoogle Scholar
[37]

M. Tegeler, O. Shchyglo, R.D. Kamachali, A. Monas, I. Steinbach, G. Sutmann

Parallel multiphase field simulations with OpenPhase

Comput. Phys. Commun., 215 (2017), pp. 173-187, 10.1016/j.cpc.2017.01.023
View PDFView articleView in ScopusGoogle Scholar
[38]

J. Gao, A. Malchère, S. Yang, A. Campos, T. Luo, K. Quertite, P. Steyer, C. Girardeaux, L. Zhang, D. Mangelinck

Dewetting of Ni silicide thin film on Si substrate: *in-situ* experimental study and phase-field modeling
Acta Mater., 223 (2022), Article 117491, 10.1016/j.actamat.2021.117491
View PDFView articleView in ScopusGoogle Scholar
[39]

S. Yang, J. Gao, M. Trini, S. De Angelis, P.S. Jørgensen, J.R. Bowen, L. Zhang, M. Chen

Ni coarsening in Ni-yttria stabilized zirconia electrodes: three-dimensional quantitative phase-field simulations supported by *ex-situ* ptychographic nano-tomography
Acta Mater., 246 (2023), 10.1016/j.actamat.2023.118708
Google Scholar

[40]

F. Grazzi, L. Bartoli, S. Siano, M. Zoppi

Characterization of copper alloys of archaeometallurgical interest using neutron diffraction: a systematic calibration study

Anal. Bioanal. Chem., 397 (2010), pp. 2501-2511, 10.1007/S00216-010-3815-4/TABLES/5
View in ScopusGoogle Scholar
[41]

A. Mehta, L. Zhou, H. Hyer, T. Huynh, B. Lu, K. Graydon, E.J. Drobner, S. H. Park, Y. Sohn

Microstructural characteristics and mechanical properties of additively manufactured Cu–10Sn alloys by laser powder bed fusion

Mater. Sci. Eng. A, 838 (2022), Article 142775, 10.1016/j.msea.2022.142775
View PDFView articleView in ScopusGoogle Scholar
[42]

R. Gu, X. Yao, D. Wang, H. Wang, M. Yan, K.S. Wong

Selective laser melting of Cu–10Sn–0.4P: processing, microstructure, properties, and brief comparison with additively manufactured Cu–10Sn

Adv. Eng. Mater., 2100716 (2021), pp. 1-10, 10.1002/adem.202100716
Google Scholar
[43]

K. Chen, C. Wang, Q. Hong, S. Wen, Y. Zhou, C. Yan, Y. Shi

Selective laser melting 316L/CuSn10 multi-materials: processing optimization, interfacial characterization and mechanical property

J. Mater. Process. Technol., 283 (2020), Article 116701, 10.1016/j.jmatprotec.2020.116701
View PDFView articleView in ScopusGoogle Scholar
[44]

J. Chen, Y. Yang, C. Song, M. Zhang, S. Wu, D. Wang

Interfacial microstructure and mechanical properties of 316L /CuSn10 multi-material bimetallic structure fabricated by selective laser melting

Mater. Sci. Eng. A, 752 (2019), pp. 75-85, 10.1016/j.msea.2019.02.097
View PDFView articleGoogle Scholar
[45]

M. Xu, H. Guo, Y. Wang, Y. Hou, Z. Dong, L. Zhang

Mechanical properties and microstructural characteristics of 316L stainless steel fabricated by laser powder bed fusion and binder jetting

J. Mater. Res. Technol., 24 (2023), pp. 4427-4439, 10.1016/j.jmrt.2023.04.069
View PDFView articleView in ScopusGoogle Scholar
[46]

N.D. Stepanov, A.V. Kuznetsov, G.A. Salishchev, N.E. Khlebova, V.I. Pantsyrny

Evolution of microstructure and mechanical properties in Cu–14%Fe alloy during severe cold rolling

Mater. Sci. Eng. A, 564 (2013), pp. 264-272, 10.1016/J.MSEA.2012.11.121
View PDFView articleView in ScopusGoogle Scholar
[47]

C. Zhang, C. Chen, P. Li, M. Yan, Q. Qin, F. Yang, W. Wang, Z. Guo, A.A. Volinsky

Microstructure and properties evolution of rolled powder metallurgy Cu-30Fe alloy

J. Alloy. Compd., 909 (2022), Article 164761, 10.1016/J.JALLCOM.2022.164761
View PDFView articleView in ScopusGoogle Scholar
[48]

S.Y. Peng, Y.Z. Tian, Y. Yang, M. Jiang, H.X. Li, J.W. Wang, S. Li, G.W. Qin

Achieving homogeneous Fe distribution and high strength in Cu-Fe composite consolidated by powder rolling

Mater. Sci. Eng. A, 884 (2023), 10.1016/j.msea.2023.145563

Google Scholar
[49]

X. Yu, Y. Song, C. Wang, K. Gu, L. Zheng, W. Qiu, B. Liu, S. Gong, Z. Li

Effect of Mg content on the microstructure and properties of high strength, high conductivity Cu-Fe-Cr-Si-Mg alloy

Mater. Sci. Eng. A, 883 (2023), Article 145510, 10.1016/j.msea.2023.145510
View PDFView articleView in ScopusGoogle Scholar
[50]

M. Wang, R. Zhang, Z. Xiao, S. Gong, Y. Jiang, Z. Li

Microstructure and properties of Cu-10 wt%Fe alloy produced by double melt mixed casting and multi-stage thermomechanical treatment

J. Alloy. Compd., 820 (2020), Article 153323, 10.1016/j.jallcom.2019.153323
View PDFView articleGoogle Scholar
[51]

L. Cen, S. Zhou, M. Gao

Controlling macroscopic segregation of the directed energy deposited Cu–Fe alloy by laser oscillation

Mater. Sci. Eng. A, 886 (2023), 10.1016/j.msea.2023.145637
Google Scholar
[52]

W. Solonick, Elastic-plastic strain acceptance criterion for structures subject to rapidly applied transient dynamic loading, (1996). https://www.osti.gov/biblio/663574.
Google Scholar
[53]

R.T. Morgan, A. Shahdin, Analysis of anchoring attachments using finite element modeling, (2020).
Google Scholar
[54]

A. Mutz, Strain limits within the scope of the integrity assessment of piping systems, (2008) 20–26.
Google Scholar

[55]

W. Kurz, D.J. Fisher, Fundamentals of solidification: fourth revised edition, Retrosp. Collect. (1998). https://api.semanticscholar.org/CorpusID:155214995.
Google Scholar
[56]

M.R. Rahul, G. Phanikumar

Solidification behaviour of undercooled equiatomic FeCuNi alloy

J. Alloy. Compd., 815 (2020), Article 152334, 10.1016/j.jallcom.2019.152334
View PDFView articleView in ScopusGoogle Scholar
[57]

G. Stechauner, E. Kozeschnik

Thermo-kinetic modeling of Cu precipitation in α-Fe

Acta Mater., 100 (2015), pp. 135-146, 10.1016/j.actamat.2015.08.042
View PDFView articleView in ScopusGoogle Scholar
[58]

H. Wen, T.D. Topping, D. Isheim, D.N. Seidman, E.J. Lavernia

Strengthening mechanisms in a high-strength bulk nanostructured Cu-Zn-Al alloy processed via cryomilling and spark plasma sintering

Acta Mater., 61 (2013), pp. 2769-2782, 10.1016/j.actamat.2012.09.036
View PDFView articleView in ScopusGoogle Scholar
[59]

Y.T. Zhu, J. Narayan, J.P. Hirth, S. Mahajan, X.L. Wu, X.Z. Liao

Formation of single and multiple deformation twins in nanocrystalline fcc metals

Acta Mater., 57 (2009), pp. 3763-3770, 10.1016/J.ACTAMAT.2009.04.020
View PDFView articleView in ScopusGoogle Scholar
[60]

Y.C. Ciou, C.L. Chang, W.H. Lu, H.K. Lin

Mechanical and microstructural properties of dissimilar copper and stainless-steel butt welds prepared using zigzag and circular fiber laser oscillation methods

Mater. Sci. Eng. A, 859 (2022), Article 144178, 10.1016/J.MSEA.2022.144178
View PDFView articleView in ScopusGoogle Scholar
[61]

Y. Li, S. Hu, J. Shen, L. Liu

Microstructures and mechanical properties of H62 brass-316L stainless steel in overlap welded joints by continuous-wave laser

Int. J. Adv. Manuf. Technol., 79 (2015), pp. 627-634, 10.1007/S00170-015-6843-6/METRICS
View at publisherView in ScopusGoogle Scholar
[62]

B.N. Kim, T. Kishi

Finite element simulation of Zener pinning behavior

Acta Mater., 47 (1999), pp. 2293-2301, 10.1016/S1359-6454(99)00069-5
View PDFView articleView in ScopusGoogle Scholar